Accepted in Materials Chemistry and Physics on 25th March 2024

Microstructure, Precipitation and Micro-segregation in Inconel 825 Weldments: A Comparative study between GTAW and EBW

Bishub Choudhury[1*], Vivek Singh[2], L. Selvarajan[3], Saurav Goel[4,5] and M. Chandrasekaran[1*]

[1]Department of Mechanical Engineering, North Eastern Regional Institute of Science and Technology (NERIST), Nirjuli, Arunachal Pradesh, India
[2]Department of Mechanical Engineering, Indian Institute of Technology, Indore, India
[3]Department of Mechanical Engineering, Mahendra Institute of Technology (Autonomous), Mallasamudram, Namakkal, Tamil Nadu, India
[4] School of Engineering, London South Bank University, SE10AA, UK
[5] Department of Mechanical Engineering, University of Petroleum and Energy Studies, Dehradun, 248007, India

*Corresponding Author: mchse1@yahoo.com, bishub.choudhury73@gmail.com

Abstract

Inconel 825 is a Ni-Fe-Cr alloy which is widely used in engineering due to its exceptional corrosion resistance and high-temperature strength. Welding (joining) of Inconel 825 has attracted strong research attention over the past few years. In this work, the effects of heat input leading to precipitation and micro segregation of Inconel 825 weldments were examined in light of comparing them while using two popular welding techniques namely, Gas tungsten arc welding (GTAW) and Electron beam welding (EBW). It was discovered that excessive heat input during GTAW can lead to root cracking and solidification cracking; while EBW demonstrated better control over undercut and maintains consistent weld quality even for higher heat inputs. Both GTAW and EBW samples exhibit dendritic grain morphologies with distinctive grain boundaries. Precipitates, such as Al_4C_3 and TiN were observed in both processes, contributing to improved mechanical properties. While GTAW weldments show some degree of segregation for Mo, Cu, Ti, and Al, EBW weldments demonstrate negligible segregation for major alloying elements but micro-segregation of Ti and Al. In general, the mechanical properties of EBW weldments was better as the average hardness, tensile strength, and ductility was much better compared to the GTAW weldments. This can be attributed to lower heat input, faster cooling rates, and a reduced rate of elemental segregation during EBW. Finally, the fractographic analysis revealed the presence of voids and micro-voids, indicating a ductile mode of failure for both GTAW and EBW samples. These findings offer invaluable insights for selecting the appropriate environment and welding method to join Inconel 825 for critical safety applications.

Keywords: Inconel 825, Micro-segregation, GTAW, EBW, Mechanical Properties

1.0 Introduction

Inconel 825 has gained considerable attention in industries due to its exceptional corrosion resistance and high-temperature strength. Some of the other notable properties possessed by Inconel 825 include high work hardening, excellent shear strength, and high chemical affinity; make it a preferred material for applications in nuclear, chemical, petrochemical, marine and automotive sectors [1]. Other than that, Inconel also find applications in aircraft industries for components such as propellers, combustion chambers, calorifier and storage tanks, thrust reversers, etc. [1-2]. Joining of materials is ubiquitous for cost-effective manufacturing and to produce a wide range of components.

Welding Inconel 825 present challenges owing to its unique metallurgical properties. Some of the challenges encompass the formation of detrimental secondary phase and vulnerability to intergranular corrosion [2-3]. To ensure the reliability and performance of welded joints in service environments, it is vital to investigate nuanced aspects of joining techniques used to weld Inconel. Conventional arc welding technique such as GMAW, GTAW and plasma arc welding (PAW) arecost-effective, simple, and portable [4-5]. However, these methods have certain drawbacks, including larger heat-affected zones, susceptibility to produce micro-fissures and a lower depth-to-width aspect ratio [5-6]. These techniques also lead to a coarse-grain morphology due to slower cooling rates involved.

Sujai and Ramkumar [7] conducted the GTAW experiments to investigate the impact of heat treatment on Incoloy 925. Direct aging of weldments resulted in 40% increase of tensile strength. Rodríguez et al. [8] examined the fatigue performance of GTAW-welded Inconel 718 specimens. A decrease in hardness in the FZ was noticed due to the segregation of Nb and Ti, leading to a reduction in fatigue strength. A study by Kumar et al. [9] suggested lower heat input for reduction in the formation of NbC and TiC precipitates and this yielded improved mechanical properties of Inconel 718 weldments. Srinivas et al. [10] investigated the impact of PAW factors on Inconel 617 weldments. An appropriate combination of parameters was suggested for optimum weld strength which was free from deleterious γ^1 phase. Chen et al. [11] examined the solidification morphology of Alloy GH3039 welded under different GTAW conditions. The heat input conditions were seen to affect the macrostructure while the microstructure in terms of columnar dendritic was dominant in the direction along the temperature gradients. The porosity formation rate was studied by Tork and Malekan [12]

under different GTAW heat input conditions during welding of C70600 alloy. Optimal control of heat input was suggested to achieve reduced porosity.

During GTAW of Inconel 718, the hot cracking tendency was studied by Xin et al. [13]. An elevated heat input led to an increased solidification cracking tendency in the weldments. Liasi et al. [14] found that during GTAW of superalloy IN939, the formation of constitutional melting in secondary and eutectic phases facilitated the existence of liquation cracking in the heat-affected zone (HAZ). The effect of filler wire in GTAW of Inconel 825 based alloy was examined by Kangazian et al. [15]. Filler wire ERNiCrMo-3 was recommended for achieving better metallurgical and mechanical properties, free from unwanted laves phases. They also employed both pulsed current and continuous current GTAW techniques for dissimilar welding of Inconel 825 and SAF 2507, utilising filler wires ERNiFeCr-1 and ER2594. Ti and Cr-rich intermetallics were identified using ERNiFeCr-1 and ER2594, respectively. The pulsed current GTAW method with ERNiFeCr-1 filler wire was recommended for better overall metallurgical and mechanical properties [16]. Ou et al. [17] utilized GTAW to weld Inconel 825-S10C steel duplex tubes with Q345R. It was observed that the increase of welding current improves metallurgical properties but degrades the pitting corrosion resistance. Sayyar et al. [18] observed weld substructure using electron backscattered diffraction (EBSD) during dissimilar welding of IN 825 and AISI 321 alloy. Deleterious Mo and Nb-rich phases were detected in the inter-dendritic regions. IN 825 showed abnormal heat-affected zone (HAZ) grain growth, whereas the AISI 321 showed nominal growth. Gope and Chattopadhyaya [19] explored the GTAW process for joining Inconel 718 with stainless steel, demonstrating a reliable joint with proper fusion, and improved strength between parent metals and filler wire. Post-weld heat treatment reduces the secondary phase and indicated that the Nickel-based filler wire was suitable to weld dissimilar joints. Thus, achieving superior weldments necessitates precise control of process parameters, regulating the optimal heat input, applying proper heat treatment strategies to attain expected mechanical and metallurgical properties.

On the other hand, advanced joining processes such as the laser beam welding (LBW) and EBW can overcome many of the challenges faced by the conventional arc welding processes but they have their own limitations [4-5]. They overcome issues such as larger fusion and heat-affected zones and achieves higher depth-to-width ratio beside lower distortion. However, susceptibility of liquation cracking and a higher rate of porosity also becomes evident. Additionally, the reactivity of electron beam with the material is a concern while

welding Ni alloys [5, 20]. Ramkumar et al. [21] examined the mechanical behaviours and collective impact of precipitation on EBW welded Inconel 625 weldments. Post-weld heat treatment with direct aging significantly enhanced the mechanical properties through the formation of γ″ strengthening phase. Vemanaboina et al. [22] performed CO_2 laser welding on Inconel 625. Higher laser power (3.3 kW) resulted in defect-free welds without any porosity. Conversely, when a reduced welding speed of 1 m/min was used, the tensile strength was found comparable to the base material. However, increase in residual stress and distortions were observed with higher heat input conditions. EBW was used by Sujai and Ramkumar [23] to create Incoloy 925 joints, where austenitic microstructure without solidification cracking was observed with HAZ liquation cracking. On comparing the as-welded joint to the direct ageing (DA), the DA condition exhibited the formation of strengthening precipitates and various carbides, resulting in improved joint efficiency (99.32%) and yield strength. Arulmurugan et al. [24] investigated the segregation effect in EBW welded superalloy 686 weldments. Elemental segregation of W and Mo was observed which led to a reduction in the ductility and toughness. Laser welding was performed by Sun et al. [25] to examine weldability-related characteristics of Inconel 617. Employing U-shaped and V-shaped filling enhances the metallurgical and mechanical properties.

Arivarasu et al. [26] successfully joined nickel-based alloy 825 using CO_2 LBW, and reported to achieve full penetration with a low heat input and demonstrating improved weld metal strength and hardness through the presence of intermetallics TiN and Al_4C_3 in the FZ. Srikanth et al. [27] conducted dissimilar welding of AISI 316L and Inconel 825 using Nd:YAG laser welding process. The laser power played a significant part in improving the tensile and hardness properties of weldments. Muthu et al. [28] studied metallurgical corrosion behaviour during dissimilar laser welding of alloy 825 and AISI 321 at 650°C in an environment involving 60% NaCl+ K_2SO_4. During hot corrosion, dichromate and sulphide phases were formed, while weight loss, along with the loss of Cr from the surface, was observed at low temperature conditions.

A comparative study between welding processes is also obligatory to gain a clear understanding of these processes, influencing parameters that have a direct or indirect influence on the resultant weld quality. Recently, Aqeel et al. [29] compared autogenous laser welding (ALW) and laser-hybrid welding (LHW) techniques while welding Inconel 617, highlighting a correlation between microstructure, hardness analysis and liquation cracking susceptibility.

LHW exhibit higher amount of low-melting eutectic phases, reduced cracking rate, and improved resistance to liquation cracking compared to ALW. Yin et al. [30] compared Inconel 625 surfacing using Cold Metal Transfer (CMT) and PAW on low-carbon steel. The findings indicated that CMT resulted in larger reinforcement and a higher dilution rate. In contrast, PAW exhibited superior surfacing forming qualities. PAW surfacing layer showed 53% higher shear strength, revealing ductile fracture characteristics, while CMT exhibits quasi-cleavage brittle fracture. A comparative study by Ren et al. [31] revealed that the CO_2 laser welding (CLW) and fiber laser welding (FLW) can have different weld bead geometries and microstructures in Inconel 617. FLW exhibits a transformation from Y-type to I-type weld bead geometry with decreased heat input, requiring lower minimum heat input for full penetration compared to CLW. Ruiz-Vela et al. [32] demonstrated that the CMT process for Inconel 625 weldments leads to improved mechanical properties, including increased tensile properties and fatigue life, compared to GTAW. The observed differences can be attributed to lower dilution and reduced particle content in the FZ due to the lower heat input provided using CMT, thus controlling the precipitation of brittle phases and enhancing the overall weld quality. Lee and Wu [33] examined the impact of welding method, cooling rate and peak temperature on the intergranular corrosion susceptibility in alloy 690. LBW with a higher cooling rate (212.6°C/s) demonstrated lower mass loss and lower reactivation current density compared to GTAW (17 to 20.6°C/s). Rapid cooling inhibits Cr-depletion and Cr-carbide precipitation along the grain boundaries, reducing corrosion in the heat-affected zone. Aqeel et al. [34] compared MIG+CO_2 laser-hybrid welding (LHW), and autogenous diode-laser (DLW) with multi-pass conventional GTAW in Inconel 617. DLW exhibited a refined microstructure and higher joint efficiency, while LHW showed highest elongation, reduced distortion and improved adaptability.

There have been studies on the effectiveness of welding techniques on various Ni-based superalloys including alloy 825 under different operating conditions. However, it is worth noting that comparative studies specifically examining the effects of GTAW and EBW on Inconel 825 are seldom reported in the literature. Fulfilling this knowledge gap, this work attempts to compare the effectiveness of GTAW and EBW of Inconel 825 under different operating conditions, to determine the most suitable conditions for reliable joining of this material. The key objective of this research was to compare and contrast the influence of heat input, precipitation and micro-segregation on the quality of welds in Inconel 825, focusing on their macrostructure, microstructure and mechanical properties when welded using GTAW and EBW.

2.0 Material and Methods

2.1 Material

The dimensions of the samples used in the study were 100 mm × 75 mm × 2.2 mm. The chemical composition of the base metal determined by X-ray fluorescence spectroscopy was Ni-41.2%, Cr-21.32%, Fe-30.4%, Cu-1.67%, Mo-3.36%, Ti-0.77%, C-0.05%, Mn-1%, Al-0.2%, Si-0.28%,. Prior to welding, all the weld specimens were shaped, thoroughly cleaned to remove the oxides . Figure 1 (a) depicts the microstructure of Inconel 825 . A fully austenitic matrix having equiaxed grains was observed. As apparent, the microstructure of Inconel 825 revealed the presence of twin boundaries (figure 1(a)), and a close inspection of the precipitates using the EDX analysis confirmed the existence of majority of titanium inside (figure 1(c)).

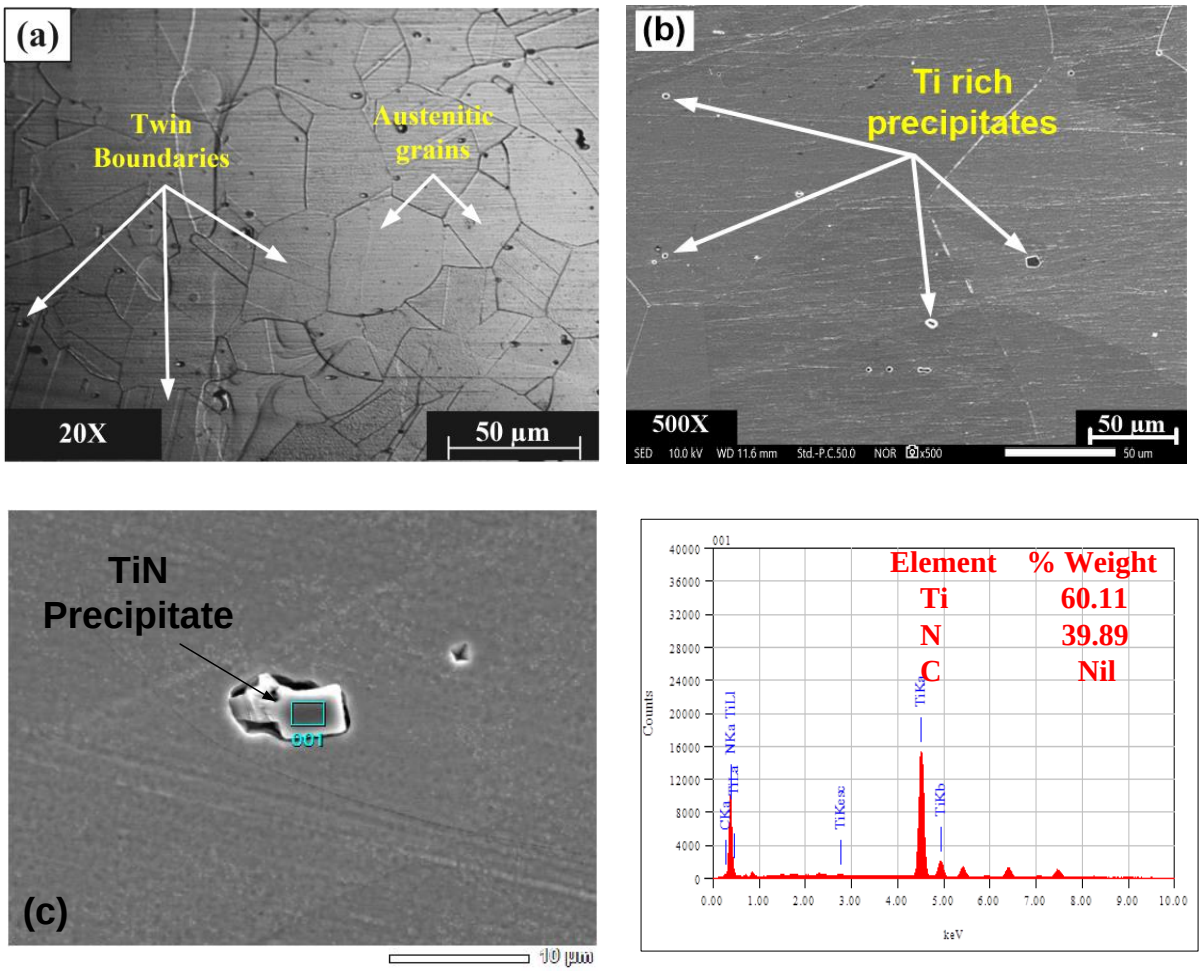

Figure 1: (a) Microstructure of Inconel 825 obtained from …, (b) Presence of Ti-rich precipitates, (c) EDX analysis confirming Ti-rich (TiN) precipitates

2.2 Experimental Setup

This work employed gas tungsten arc welding (GTAW) (MIGATRONIC PI 350 PLASMA) and electron beam welding (EBW) (12KW-EBW). The samples were clamped as shown in figure 2 to avoid the distortion during welding. Pilot experiments were done to identify the optimal welding parameters. The experimental setup used for GTAW and EBW is shown in figure 2 along with the clamping setup.

Initially, GTAW experimentations were carried out for three different heat input settings considering arc efficiency of 0.78%. Table 1 shows the GTAW welding parameters used for three experimental runs. To protect the weld pool from oxidation, argon gas having 99.9% purity was used. 60^{o} torch angle and 2.5 mm electrode diameter were used. Similarly, EBW experimentations were also carried out considering four important EBW parameters at three different heat input settings shown in table 2. A constant gun chamber vacuum of 3.6x10^{-7} mbar and work chamber vacuum of 4.2x10-4 mbar was maintained throughout the experiments. Filament current of 65 mA, beam focus current of 3.2 mA and oscillation diameter of 1 mm were kept constant during the EBW investigation. Both GTAW and EBW experiments were conducted autogenously, i.e. no additional filler material was utilized during the experimental process.

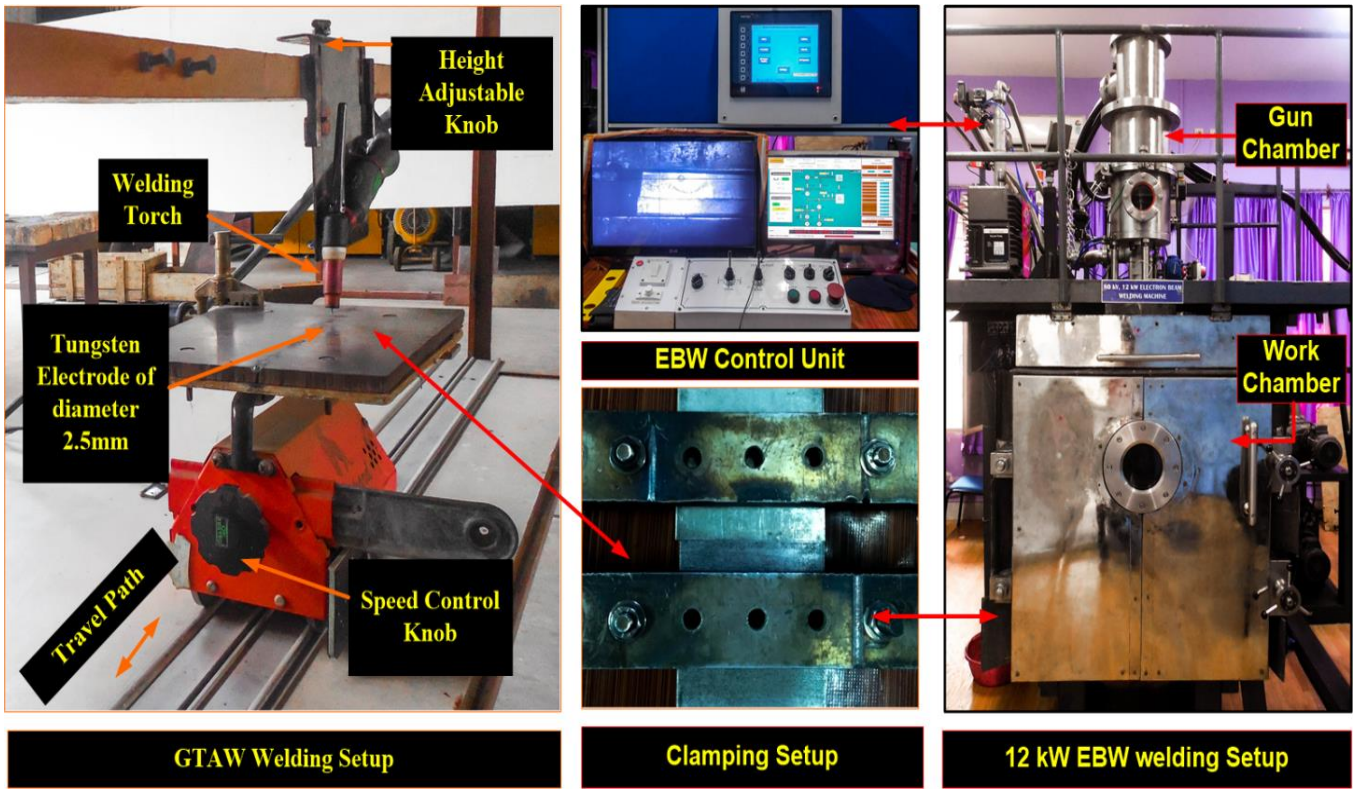

Figure 2: GTAW and EBW welding setup

Table 1: Welding parameters for GTAW samples

Sample	Welding current (*I*), (A)	Welding speed (*S*), mm/min	Gas flow rate (*G*), l/min	Arc length (*N*), mm	Heat input, kJ/mm
1	100	205	12	2.0	0.342
2	120	205	9	2.0	0.411
3	120	180	9	2.5	0.468

Table 2: Welding parameters for EBW samples

Sample	Acceleratin g voltage (*V*), kV	Welding speed(*S*), mm/min	Beam current(*I*), mA	Beam oscillatio n(*O*), Hz	Heat Input, kJ/mm
1	48	1200	38	200	0.091
2	54	1050	42	400	0.130
3	60	900	46	600	0.184

2.3 Metallographic and mechanical characterization

The cross-sectional profiles of the welded specimens were cut using WEDM to prepare test samples as per the scheme shown in figure 3. Standard metallographic procedures were followed including polishing with an emery paper, involving aluminium slurry and etching with 5ml HCL + 7.5mL HNO_3 + 5mL Acetic acid mixture. The macrographs were initially analysed visually, with three measurements taken for each weld bead using a NIKON SMZ 25 Stereo microscope. Non-destructive testing was then conducted to assess possible weld defects. The metallurgical aspects of the weldments were determined using an inverted optical (Carl ZEISS) and scanning electron microscope (SEM) (JSM-IT300). To perform precipitation and segregation study, SEM/EDX examination was carried out on Inconel 825 weldments.

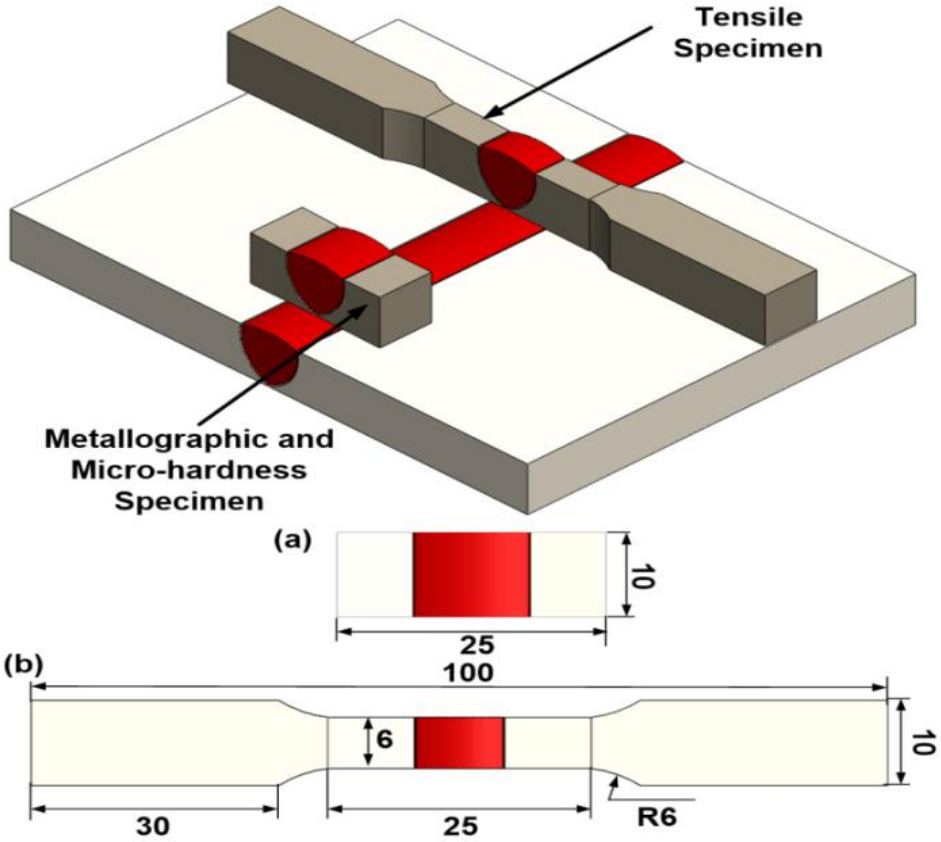

Figure 3: Extraction of samples for (a) Metallographic examination, (b) Tensile Testing

The samples prepared for metallographic analysis were further utilized for microhardness investigation following the standard ASTM E92, involving a digital Vicker microhardness tester. 0.5 kg was applied on all specimens for 10 seconds. The welded specimens were also tensile pulled in accordance with the ASTM E8M standard. INSTRON 8801 testing machine was used to conduct the tensile test with a crosshead speed of 1 mm/min. The ultimate tensile strength (*UTS*), percentage elongation (%*E*) and yield strength (*YS*) values were directly extracted.

3.0 Results and discussions

3.1 Macrostructural analysis

The transverse and longitudinal macro-structural cross-sectional view of GTAW welded Inconel 825 weldments are shown in figure 4, under three different test conditions. Table 3 provides quantifiable data into the variations observed in the heat input and the resulting changes in penetration and the area of the weldment. Figure 5 highlights atrend in the variations, considering the mean value of each weld bead parameter.

Table 3: Weld bead characteristics for GTAW samples

Sample	Heat Input (kJ/mm)	Penetration (mm)	Weldment area (mm^2)
Sample 1	0.342	2.089±0.013	8.250±0.253
Sample 2	0.411	2.325±0.020	11.148±0.510
Sample 3	0.468	2.358±0.016	11.929±0.447

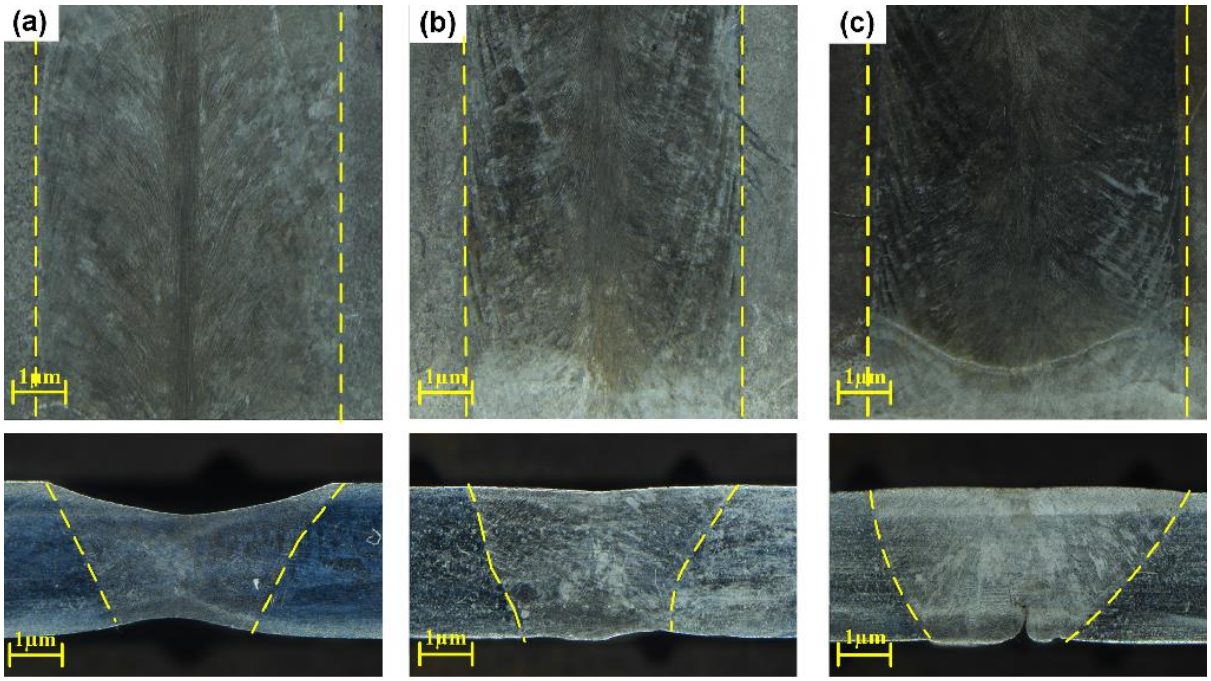

Figure 4: Cross-sectional view of GTAW welded Inconel 825 of: (a) sample 1; (b) sample 2; (c) sample 3.

In figure 4 (a), the cross-sectional of the welded sample for aheat input of 0.342 kJ/mm is illustrated. The macro graph revealed a mean weldment of area 8.250mm^2 with incomplete penetration (2.089mm). This lake of penetration is primarily owing to the lower heat input per unit length which causing reduced amount of molten metal in the weld pool. Conversely, when the heat input was increased to 0.411kJ/mm (figure 4 (b)), full penetration (2.325mm) is achieved, covering a mean weldment area of 11.148 mm^2. The weld is free from known cracks and microfissuring as observed in non-destructive testing. The weld exhibits good sidewall fusion without any indication of undercut, spatters, surface porosity, etc. Further increase of heat input to 0.468KJ/mm, the mean weldment area is increased further to 11.929 mm^2 with full penetration (2.358mm) (figure 4 (c)). However, the presence of defects such as root cracks and solidification cracks is observed in the weldment. Occurrence of ‘root crack’ is due to the low current at the beginning or due to hydrogen embrittlement. Generally, Inconel 825 is

susceptible to hydrogen-assisted fracture and low-temperature crack propagation [1-2]. To prevent such defect, appropriate filler material with higher initial current setting is recommended. Also, nickel based alloys are prone to 'solidification crack,' which may be eliminated considering pre-homogeneous heat treatment or lower heat input [2]. Formation of other defects like an undercut, porosity, and any sort of transverse crack was not witnessed.

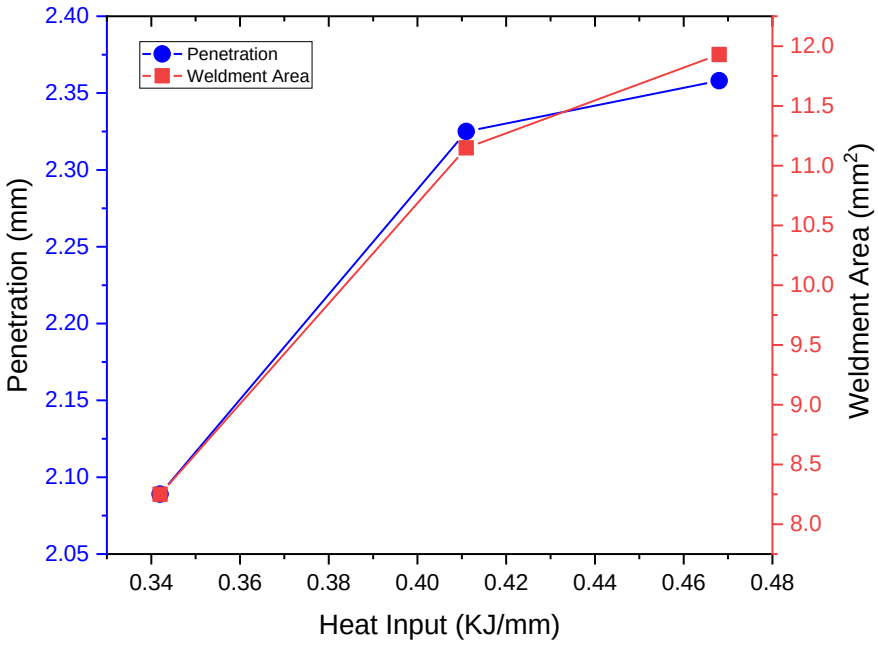

Figure 5: Effect of heat input on the penetration and weldment area for GTAW samples.

For the EBW welded Inconel 825 specimens, the transverse and longitudinal macro-structural cross-sectional view are illustrated in figure 6 under three different test conditions. Table 4 and figure 7 demonstrates the relationship between the change in heat input and the corresponding variations in penetration depth, weldment area and undercut tendency.

Table 4: Weld bead characteristics for EBW samples

Sample	Heat Input (kJ/mm)	Penetration (mm)	Weldment area (mm^2)	Undercut (mm)
Sample 1	0.091	1.40±0.026	3.24±0.317	0.151±0.003
Sample 2	0.130	2.34±0.060	5.38±0.091	0.063±0.000
Sample 3	0.184	2.35±0.023	6.07±0.466	0.012±0.000

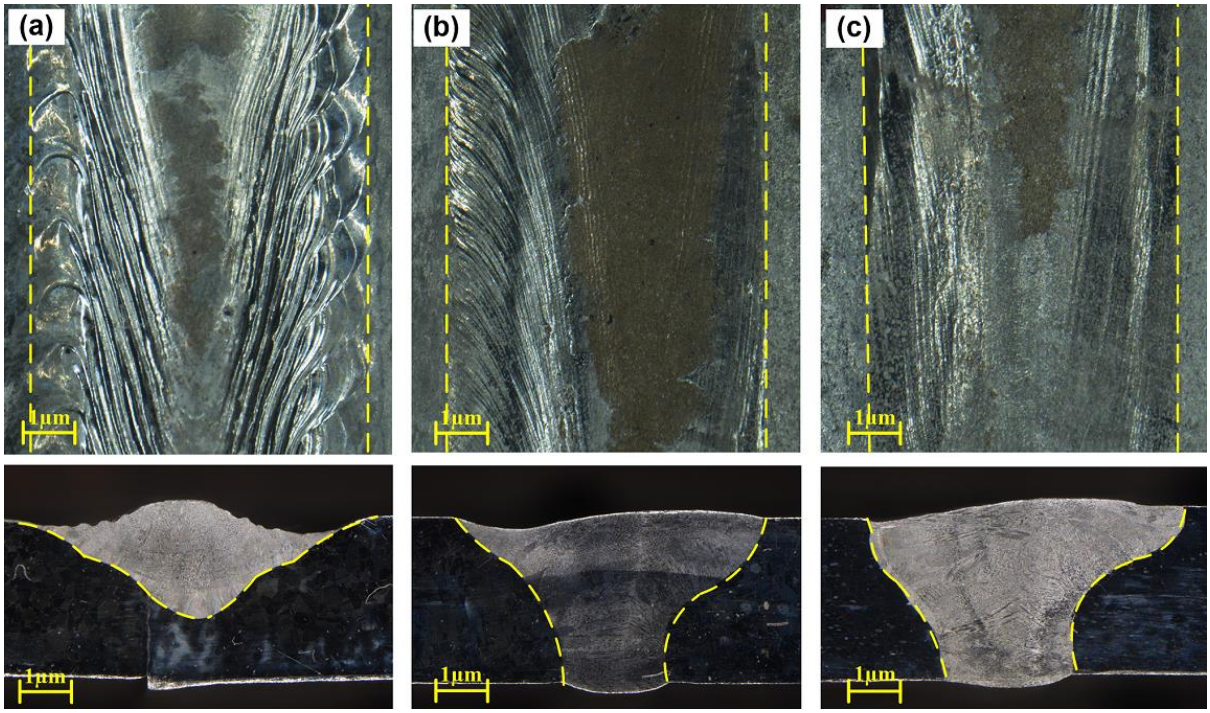

Figure 6: Cross-sectional view of the EBW welded Inconel 825 of: (a) sample 1; (b) sample 2; (c) sample 3.

The figure 6 (a) shows the macro-structural cross-sectional view of sample 1 with lowest heat input of (0.091kJ/mm) which produces a mean fusion zone area of 3.24mm^2 with mean penetration 1.40mm resulting in a mean undercut of 0.151mm. This insufficient penetration observed in the weldment primarily stems from the lower heat input per unit length, a consequence due to heat-transfer occurring in the conduction mode. The presence of undercut is also quite evident in the weldment. This occurrence is a common phenomenon in EBW and LBW welds, primarily caused by the expulsion or evaporation of a small quantity of molten material [35-36]. The sample welded at intermediate heat input (0.130 kJ/mm) is depicted in Figure 6 (b). Full penetration of 2.34mm with a weldment area of 5.38mm^2 is observed. The transition from conduction to keyhole heat transfer mode, facilitated by the increased heat input, is responsible for achieving full penetration in the weld. The presence of nominal undercut of 0.063mm is observed which is lower than the allowable undercut of 0.07T for a class-A weld (where T is thickness of the plate) [37].

Further increase in heat input to 0.184kJ/mm^2, results to a mean weldment area 6.07mm^2 with full penetration of 2.35mm (figure 6 (c)). The undercut in the sample is quite nominal of 0.012mm. The decrease in undercut observed in both sample 2 and sample 3, in relation to sample 1, can be attributed to a more uniform heat distribution and improved blending of the weld metal [38]. All the samples exhibit good sidewall fusion without any form

of microfissuring and porosity. The width of the weld is approximately 50% greater in the upper or cap section compared to the lower or root sections. This phenomenon can be ascribed to the cap region absorbing a larger quantity of heat from the beam source in contrast to the root portion.

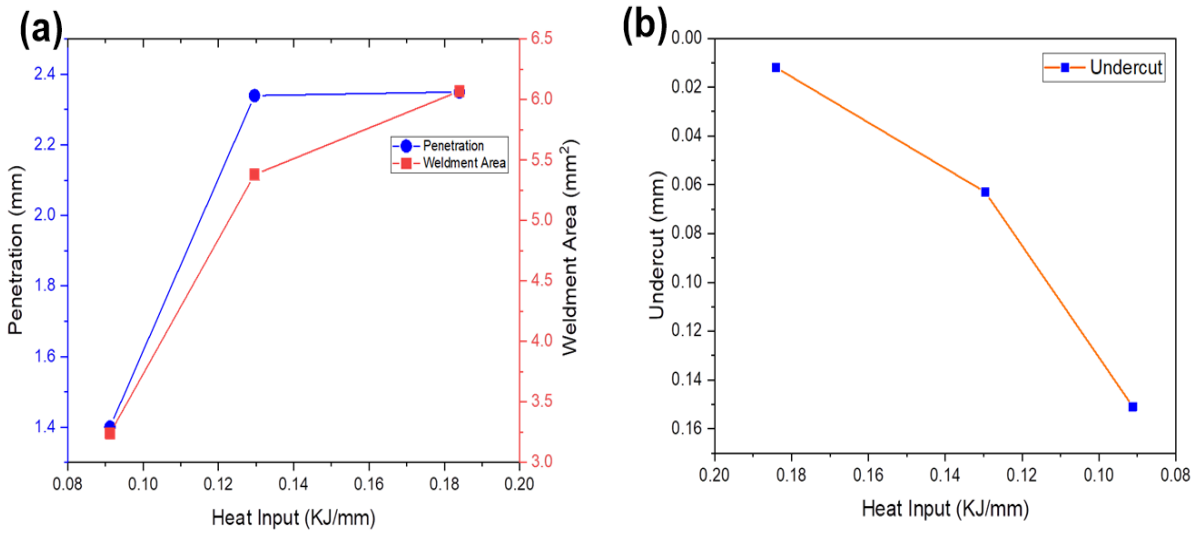

Figure 7: Heat input vs. (a) Penetration and weldment area. (b) Undercut tendency

When comparing the two welding processes, it is crucial to have the right amount of heat input in order to create weld beads that are defect-free. Both GTAW and EBW benefit from intermediate heat input, which leads to improved weld bead geometry without welding defects such as surface porosity, undercut, or microfissuring. However, when the heat input is at its highest in GTAW, there is a risk of root cracking and solidification cracking. Conversely, the lowest heat input condition in EBW exhibits the highest tendency for undercut.

3.2 Weld interface microstructure

The interfacial morphology for all the GTAW weldments are shown in figure 8 (a-d). In each of the three instances, the HAZ exhibits an increase in the size of austenitic grains. As the HAZ extends away from the fusion line towards the base metal, there is a transition in grain size, shifting from larger, coarser grains to smaller, finer grains. There is a noticeable thickening of grain boundaries in the HAZ near the FZ. This is primarily because of the presence of various alloying elements particularly titanium. During solidification, these Ti lowers the melting point and form low-melting carbide-austenite eutectics [39-40]. Moreover, thickening of grain boundaries results in liquation cracking in weldments which are not observed in the microstructural analysis. The presence of an unmixed zone (UZ) adjacent to

the FZ is not witnessed which generally occurs due to the compositional difference between the filler material to the base metal [2-3]. As evident in autogenous welding process, the occurrence of epitaxial growth is lucid from the base metal to FZ. This epitaxial growth on partially melted grains transpires through the consumption of liquid metal, effectively preventing the creation of an UZ and minimizing the adverse metallurgical consequences associated with the galvanic couple.

An increase in heat input also results in a slight enlargement of grain size within the HAZ, leading to coarser grains compared to those in the base metal. According to Dupont et al. [2], the extent of grain growth in the HAZ of nickel-based alloys with solid-solution strengthening depends on both the heat input and initial grain size of the base metal employed during the welding process. Furthermore, two important aspects that dictate the solidification microstructure is temperature gradient (G) and growth rate (R) in the FZ [41]. The morphological structure is obtained by the G/R ratio, whereas the grain structural size is influenced by the multiplication of G and R, representing the cooling rate [41, 2]. Here, the presence of dendritic grain growth is evident which may due to lower G/R ration. With the movement towards the weld centre, epitaxial growth changes to the dendritic with the decreasing (G/R) ratio [41].

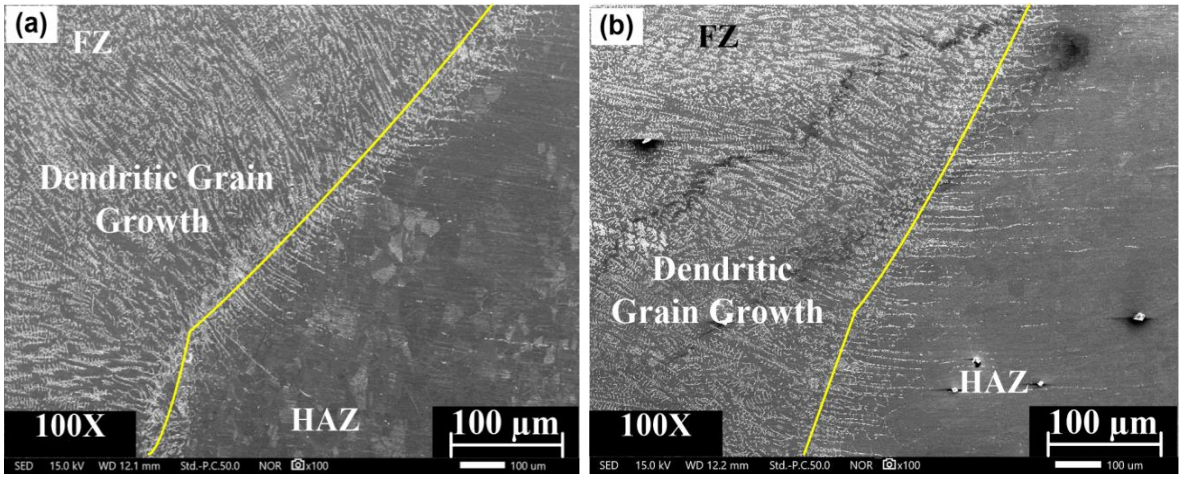

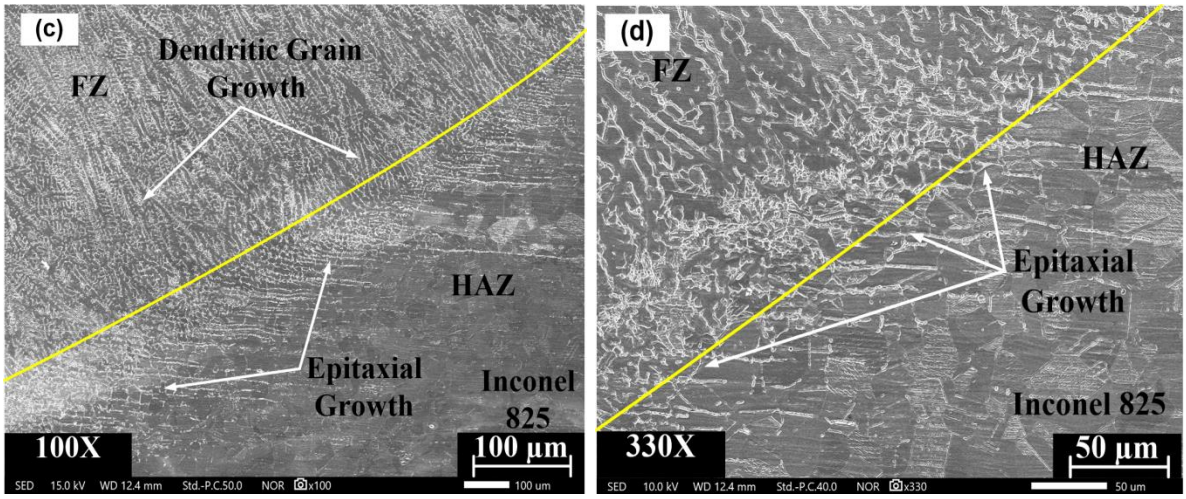

Figure 8: Microscopic examination of the GTAW weld interfaces: (a) Sample 1 exhibits dendritic grain growth and HAZ; (b) Sample 2 displays dendritic grain growth, HAZ, and epitaxial growth; (c-d) Samples 3 shows dendritic grain growth, HAZ, and epitaxial growth at magnifications of 100X and 330X, respectively.

The interface morphology of the EBW weldments is illustrated in figure 9. Similar to GTAW welded weldments, epitaxial nucleation is apparent at the fusion line, a phenomenon commonly observed in autogenous welding and processes involving both matching and non-matching filler materials [2, 41]. This epitaxial growth plays a pivotal role in mitigating the adverse metallurgical effect of the galvanic couple, particularly in conventional welding processes that employ additional filler wire. The HAZ grain growth is found negligible in the first and second samples, while it is slightly noticeable in the sample welded using the highest heat input condition. However, this HAZ grain growth is considerably less than the grain growth observed in the samples welded using GTAW. The reduced HAZ grain growth can be ascribed to the EBW process's lower overall heat input that leads to a higher depth-to-width ratio, faster cooling rate, and more uniform heat dispersion. Furthermore, the absence of detrimental structures such as the unmixed zone is notable at the base metal-FZ interface.

EBW and LBW typically result in higher thermal gradients, leading to the development of complex microstructures due to non-equilibrium conditions following the rapid solidification of the FZ. Across the weld, the thermal gradient is at its minimum in the centre and reaches its maximum at the fusion line [41-42]. Consequently, the proportion of G relative to R is significantly elevated near the fusion line and progressively diminishes as it moves toward the weld center. This results in the visible growth of cellular and columnar dendrites near the fusion line, believed to occur perpendicular to the weld boundary and aligned with the direction of heat flow along the <100> orientation [38, 42]. As the G/R ratio declines, there is

a shift in the substructural appearance within the central area of the FZ of the weld, transitioning from columnar and cellular dendrites to equiaxed dendrites. The fine structure of equiaxed dendrites during EBW can be attributed to the accelerated cooling rate due to the elevated G.R rate [2, 38].

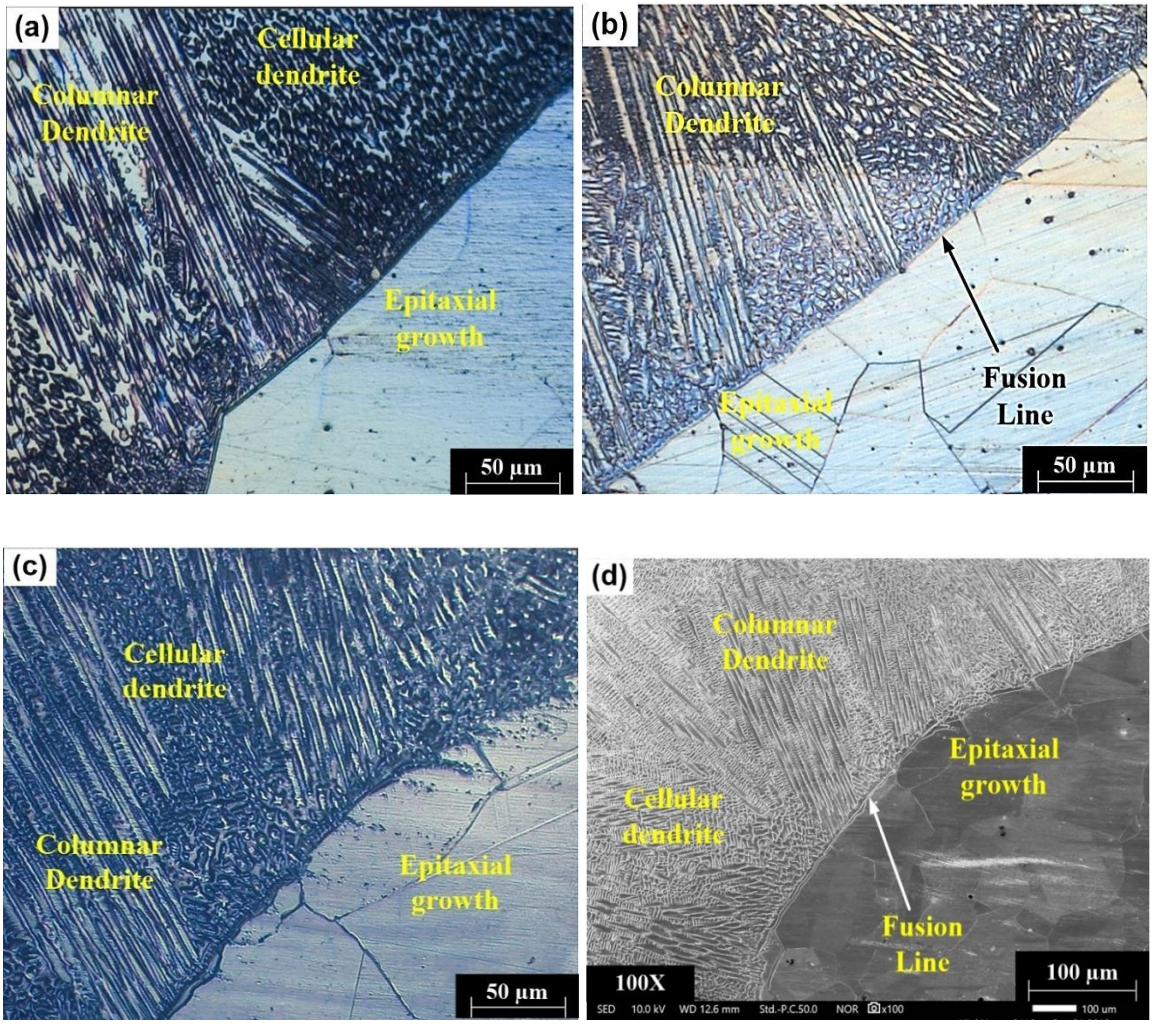

Figure 9: EBW weld interface microstructure showing dendritic grain morphology, clear fusion line and epitaxial growth for: (a) sample 1; (b) sample 2; (c-d) sample 3.

3.3 Fusion zone microstructure

The FZ microstructures of the GTAW weldments are depicted in figure 10, showcasing dendritic grain morphology. Within the dendritic structure, three main types are identified: cellular, equiaxed, and columnar as depicted in the figure 10. The presence of three distinctive grain boundaries is evident in the FZ microstructure namely solidification subgrain boundaries (SSGBs), solidification grain boundaries (SGBs) and migrated grain boundary (MGBs). The SSGBs are characterizes as low angle boundaries and are evident in all three cases of weldments. These boundaries, which divide one subgrain from another, are formed as a result

of solute redistribution. These subgrains are primarily present in cellular or dendritic forms, as evidenced in the FZ microstructure. The formation of SGBs is the result of the competitive grain growth in weld pool. These boundaries occur at the intersection points of groups of subgrains [2, 43]. The occurrence of MGBs are only observed in the lower heat input sample which are absent in second and third case of weldments. These MGBs are form due to the migration of crystallographic components from the compositional component at the end of solidification. The segregation of alloying element is quite possible along these grain boundaries [41, 43].

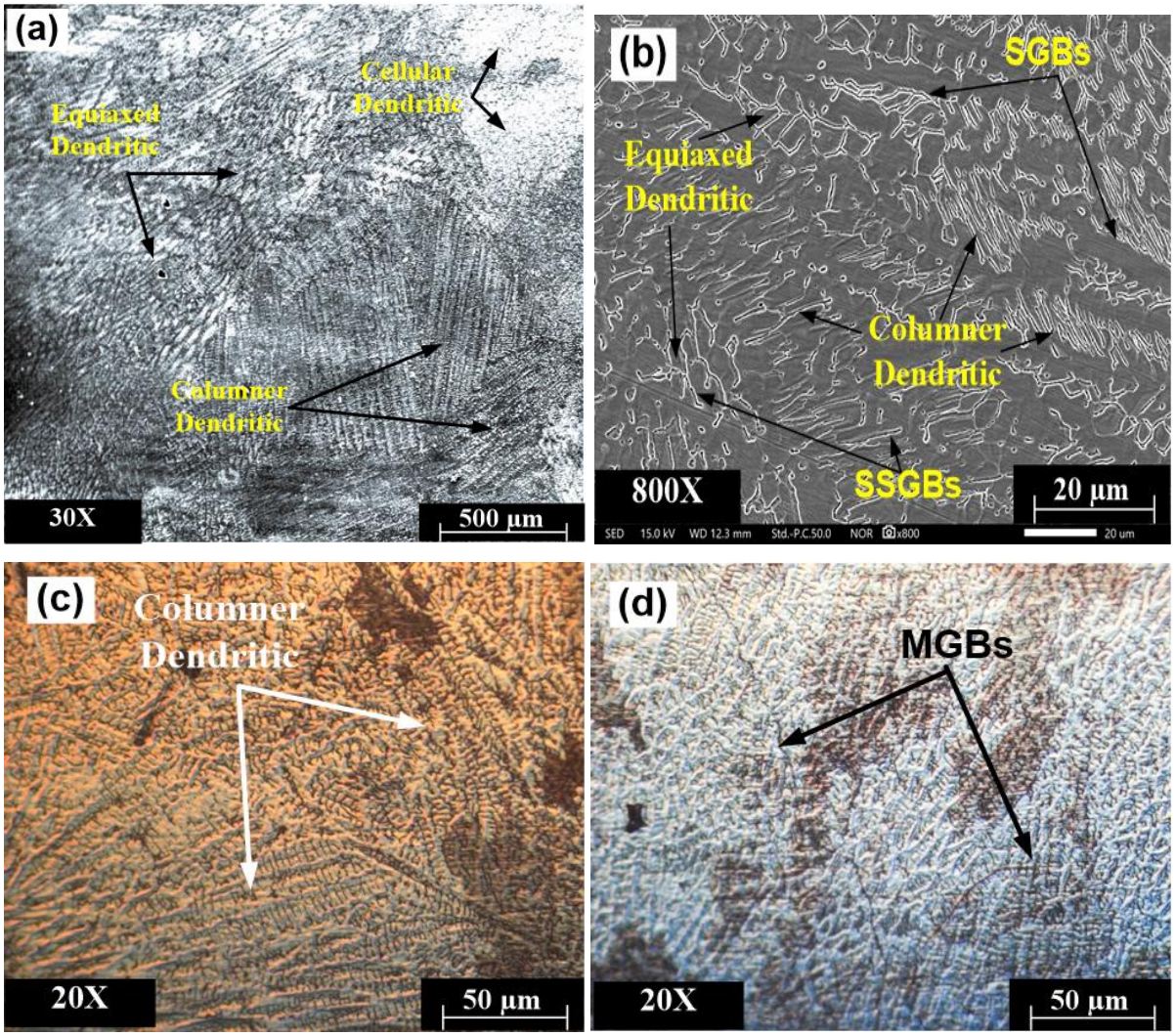

Figure 10: GTAW fusion zone microstructure showing: (a-c) different grain morphology and boundaries; (d) migrated grain boundaries (MGBs) in sample 1.

The FZ morphology for EBW welded samples are illustrated in figure 11 (a-e). The grain shape appears to be cellular and columnar dendritic in nature near the fusion line as well as in other parts of the FZ. The grain morphology at the weld center exhibits fine equiaxed

dendritic type morphology, which is dominant in the root and middle portions due to the smaller area and faster cooling rate with a higher G.R rate. The presence of deleterious liquatation cracking and any other form of microfissuring is not evident in FZ microstructure. The FZ reveals the occurrence of well-defined grain boundaries consisting SGBs and SSGBs. Similar to GTAW welded samples, the occurrence of deleterious MGBs is not observed in the fusion zone microstructure, ensuring better metallurgical characteristics by eliminating the 'sweeping mechanism' and ensuring less microsegregation. Figure 11 (d) and (e) clearly illustrate FZ microstructure having distinct primary dendrite arm spacing (DAS), secondary dendrite arm spacing (SDAS), and tertiary dendrite arm spacing (TDAS). The dendritic arm spacing, specifically seen in the middle and upper sections, is primarily attributed to the reduction in heat input from the cap to the root of the weldment [38, 43].

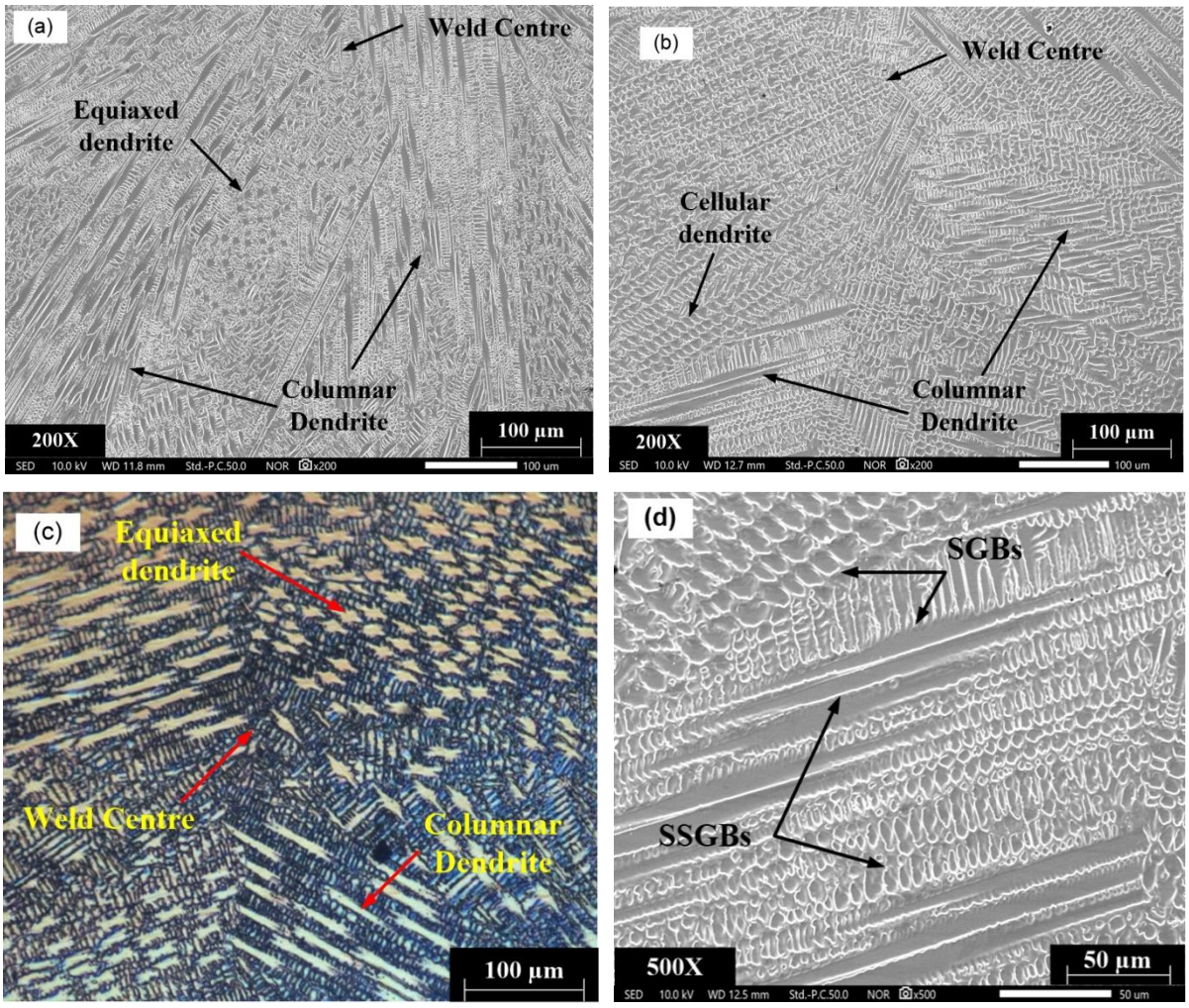

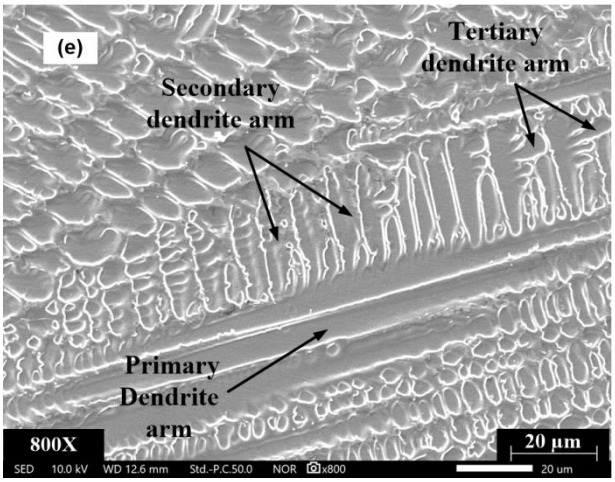

Figure 11: (a-c) EBW fusion zone microstructure of samples 1, 2, and 3 illustrating grain morphology in the weld center, respectively; (d) distinct grain boundaries, (e) dendritic arm morphology.

3.4 Precipitation and Micro-segregation study

SEM/EDX investigation was conducted to determine the existence and composition of precipitates using both GTAW and EBW processes. Intergranular and intragranular precipitates were observed in the FZ, interface, and base metal microstructure. Inconel 825, comprising Cr-21.32%, Ti-0.77%, C-0.05%, and Al-0.2%, suggests the formation of carbide precipitates in high-temperature conditions. The SEM/EDX analysis identifies these precipitate as secondary phase precipitate Al_4C_3 (Figure 12 (a)) which helps in restricting grain boundary sliding. This increases creep and flexural strength of the weldments [1-2]. The presence of Ti-rich precipitates like TiN (figure 12 (b)) is also identified. The presence of this beneficial precipitate eliminates the tendency for the formation of porosity [15, 21].

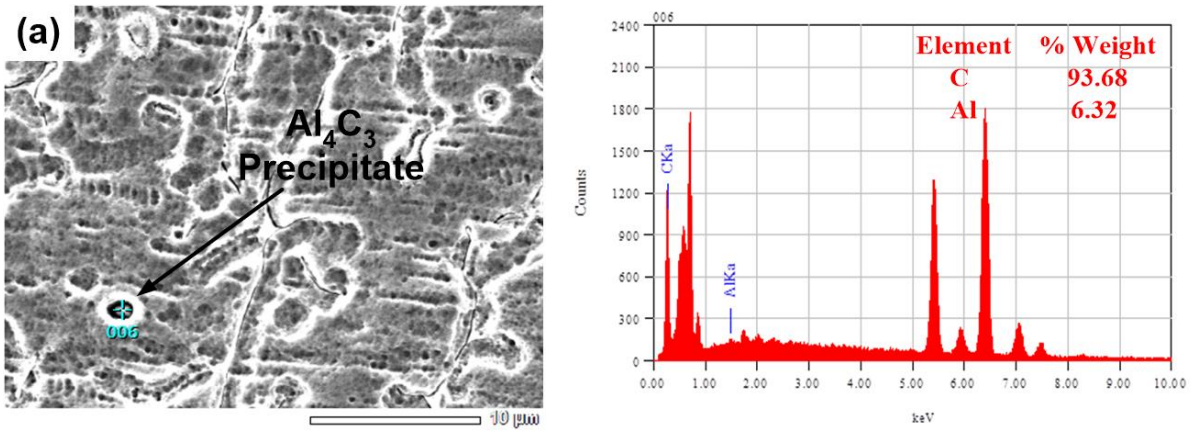

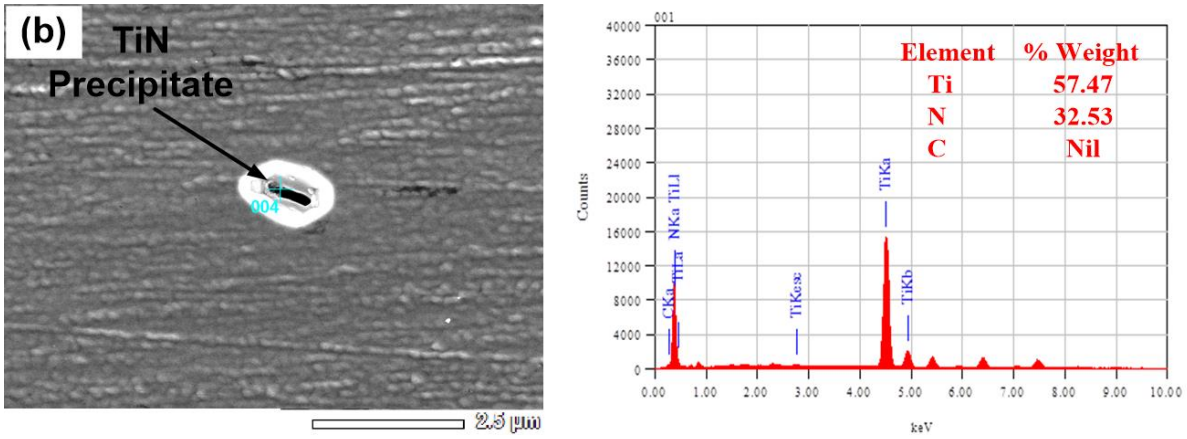

Figure 12: SEM/EDX analysis showing presence of precipitate (a) Al_4C_3; (b) TiN

To study the micro-segregation behaviour of alloying element, point EDX analysis was carried out in dendritic core and dendritic grain boundaries. The Scheils's equation [35] is used to study and analysis the coefficient of segregation (k), as expressed below:

$$k = \frac{C_c}{C_b} \tag{1}$$

where, C_c represents the concentration of element at grain matrix (core) and C_b represents the concentration of element at dendritic boundary. Here, the degree of micro-segregation increases with the decreasing k value (for k<1) [2, 4].

Segregation analysis for the GTAW weldments was conducted on samples 2 and 3. The SEM/EDX results for these samples are depicted in Figure 13 (a), (b) and Figure 14 (a), (b), respectively. The computed segregation coefficient for both samples is presented in Table 5. The k-values for the primary alloying elements Ni and Fe are both equal to 1, indicating minimal segregation throughout the weldment, consistent with findings reported by Ren et al. [31]. The k value for Cr is near to unity suggesting negligible segregation of elements enriched with Cr. The calculated segregation coefficient for Mo, Ti, Cu, and Al elements is lower for sample 3 than sample 2. This implies that the sample 3 has higher segregation of element enriched with Mo, Ti, Cu, and Al. This segregation leads to the creation of precipitates within the inter-dendritic regions of the weld zone, as previously mentioned.

Another noteworthy finding from the study is the existence of niobium (Nb) in the grain boundary matrix, which was not detected within the inter-dendritic gaps. This suggests that segregation of Nb is absent which generally segregate to the inter-dendritic areas upon solidification. Additionally, this absence of Nb-rich Laves phase eliminates the adverse

metallurgical impact that can reduce mechanical properties by inducing microfissures in weldments. [44].

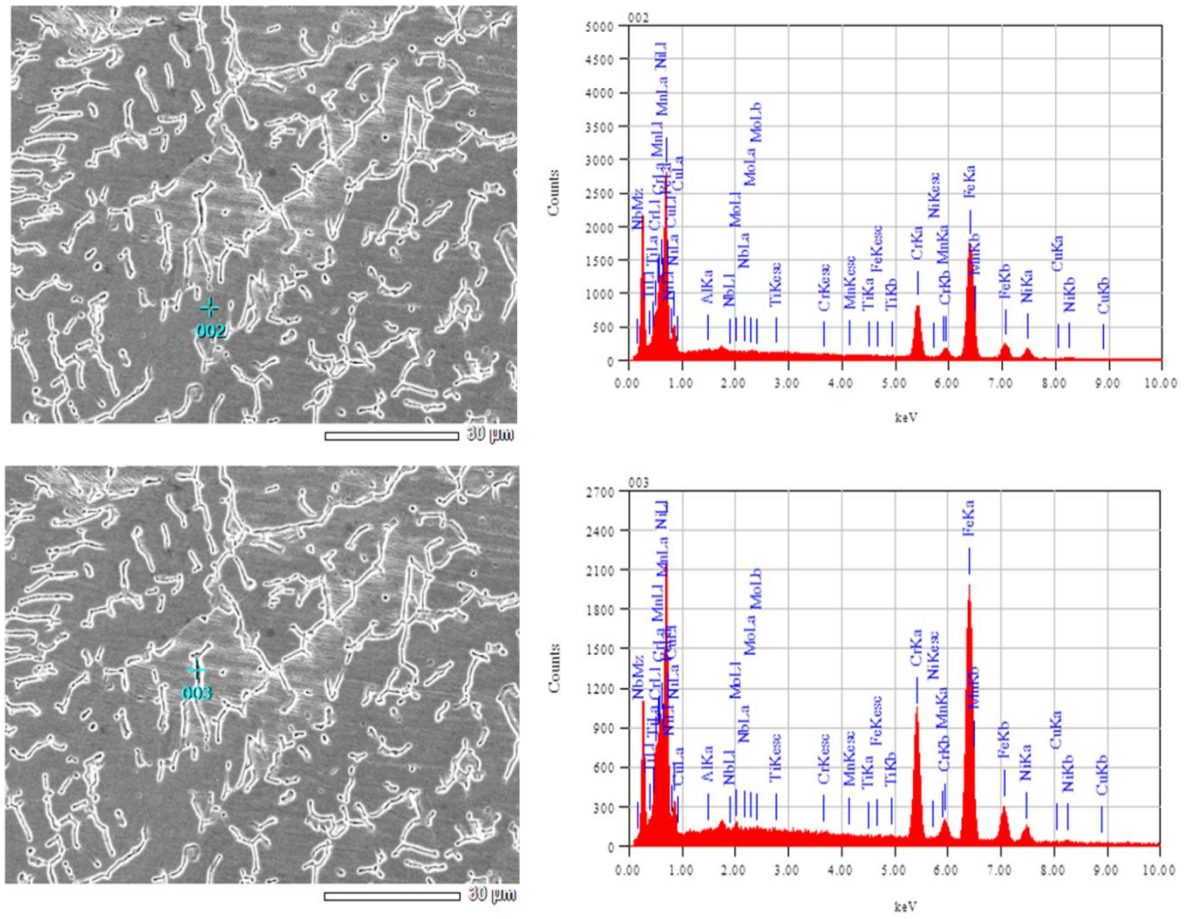

Figure 13: SEM/EDX point analysis for sample 2 at the (a) grain matrix; (b) grain boundary.

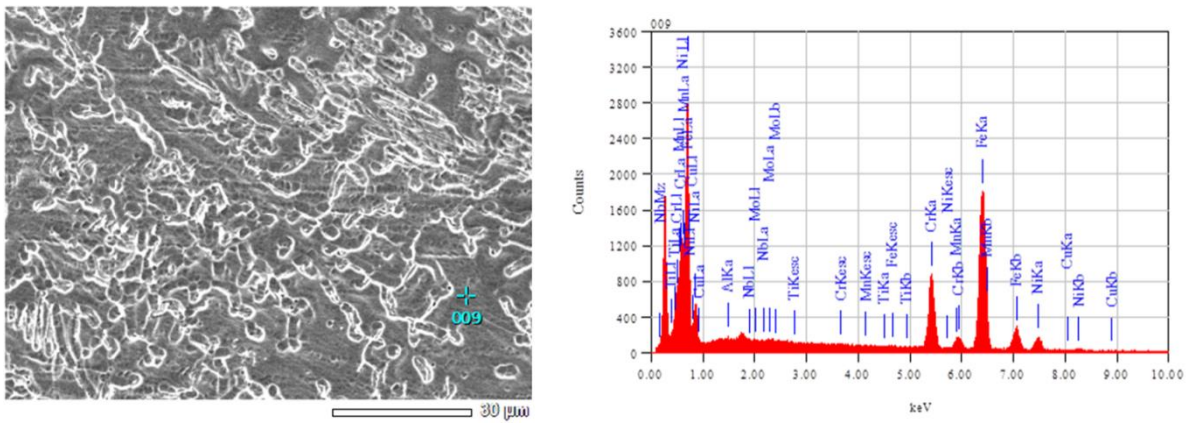

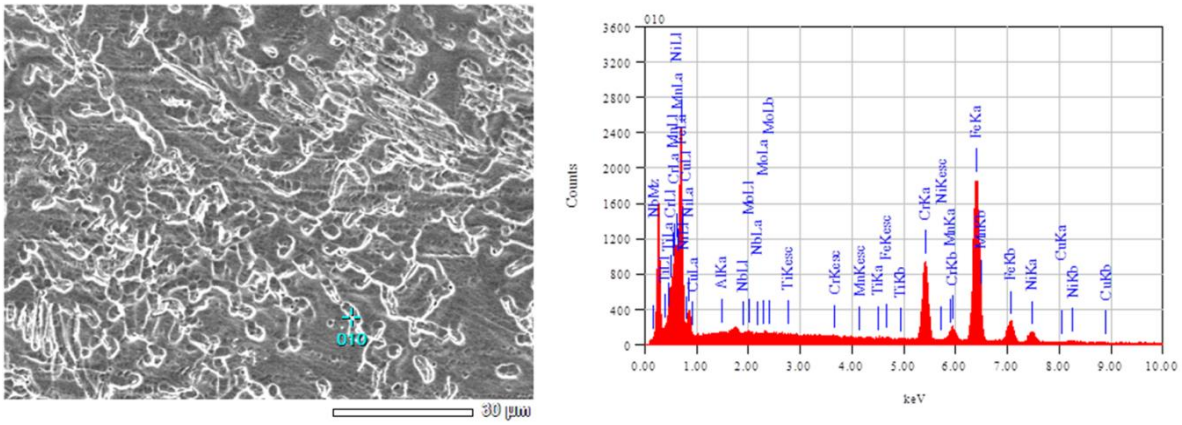

Figure 14: SEM/EDX point analysis for sample 3 at the (a) grain matrix; (b) grain boundary.

Table 5: Result of SEM/EDX analysis for GTAW sample (2 and 3)

	Elements	Ni	Cr	Mo	Fe	Cu	Ti	Al	Nb
Sample 2	C_c	40.21	17.81	2.38	28.89	1.14	0.17	0.02	0.10
	C_b	39.83	19.39	2.25	28.68	1.08	0.19	0.03	-
	k	1.01	0.92	1.05	1.00	1.05	0.89	0.66	-
Sample 3	C_c	39.89	17.81	2.33	28.43	1.11	0.15	0.04	0.26
	C_b	39.67	18.93	2.68	28.19	1.33	0.20	0.07	-
	k	1.00	0.94	0.86	1.00	0.83	0.75	0.57	-

To study the micro-segregation of alloying elements in EBW samples, SEM/EDX analysis was carried out, as depicted in Figure 15. The observed results are summarized in Table 6. The weight percentages of primary alloying elements like Ni, Fe, and Cr are all equal to 1, indicating minimal segregation throughout the weldment. Micro-segregation of elements such as Ti, and Al has occurred for all three samples which lead to formation of precipitates like TiN, Al_4C_4 in the inter-dendritic areas of weld metal [38, 44]. The segregation of Nb within the interdendritic spacing of columnar grains is expected, which can result in the development of secondary phase precipitates like NbC or laves phase. Further analysis using transmission electron microscopy is necessary to investigate these precipitates in more detail. Overall, a higher rate of micro-segregation was observed in the GTAW welded samples compared to the EBW welded samples.

Table 6: SEM/EDX elemental analysis results for EBW samples

Unit	Ni	Cr	Mo	Fe	Cu	Ti	Al	Nb

Sample 1	C_b	39.67	22.37	2.73	30.59	1.62	0.70	0.23	0.11
	C_c	39.87	22.68	2.74	30.39	1.81	0.64	0.21	0.04
	K	1.01	1.01	1.00	0.99	1.12	0.91	0.91	0.36
Sample 2	C_b	39.34	22.48	3.01	30.17	1.90	0.66	0.18	0.18
	C_c	39.71	22.19	2.97	30.00	1.89	0.60	0.15	0.04
	K	1.01	0.99	0.99	0.99	0.99	0.91	0.83	0.22
Sample 3	C_b	38.66	22.12	2.93	30.01	1.88	0.73	0.23	0.08
	C_c	38.72	21.82	2.89	29.65	1.89	0.65	0.21	0.01
	K	1.00	0.99	0.99	0.99	1.01	0.89	0.91	0.13

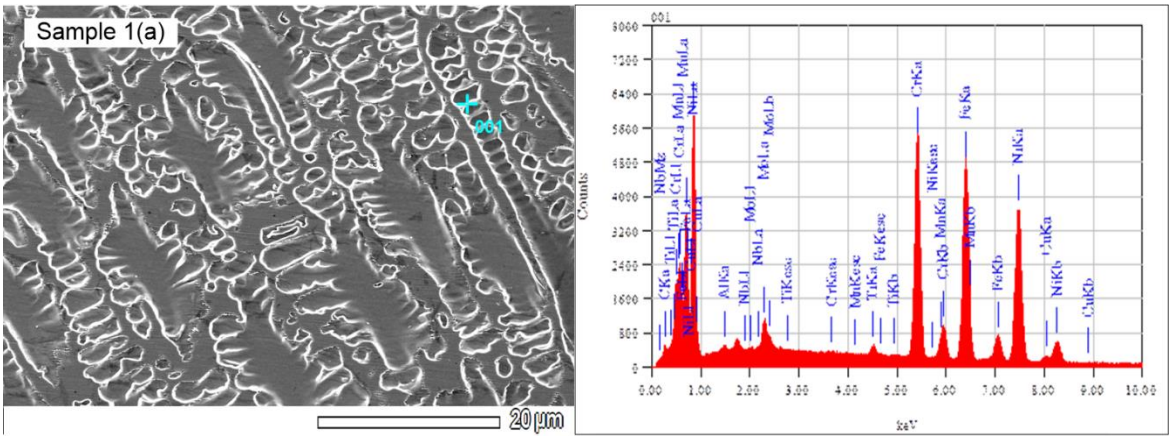

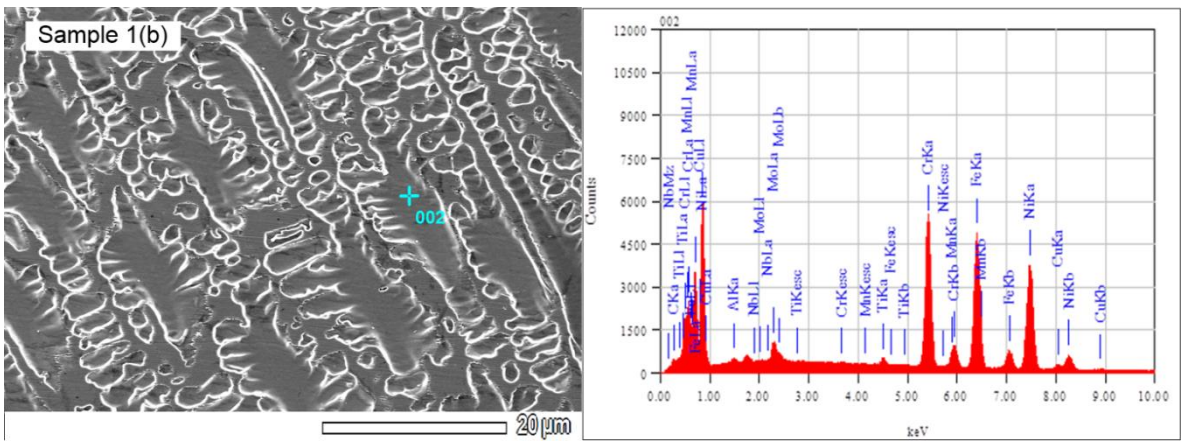

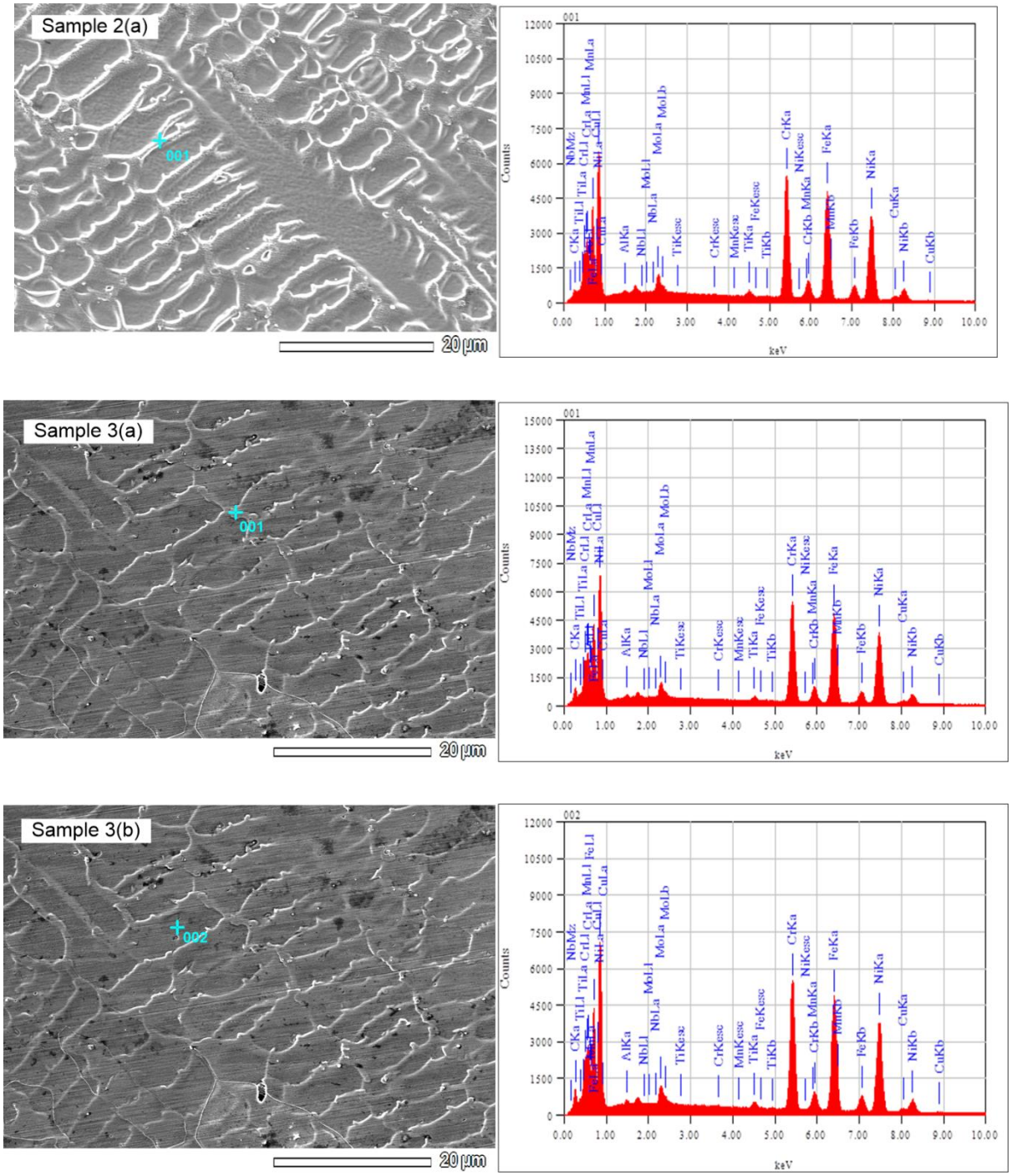

Figure 15: SEM/EDX area analysis for sample 1, 2 and 3 at (a) grain boundary; (b) grain matrix

3.5 Micro-hardness Investigation

Figure 16 illustrates the micro-hardness plots for the GTAW welded samples, and the findings are provided in Table 7. The average micro-hardness for Inconel 825 is found as 172 HV. The average fusion zone hardness for sample 1 at the cap and root portion is recorded as 168 HV and 171 HV respectively resulting an average hardness of 169.5HV, which is lower than the hardness of base metal. For sample 2, both the cap and root sections of the FZ exhibit

micro-hardness values of 173 HV and 177 HV, respectively. Similarly, for sample 3, 172 HV, and 175 HV are recorded for the cap and root portion respectively, which are marginally greater than the parent metal. This increase in average hardness in samples 2 and 3 can be ascribed to the elevated heat input, facilitating the formation of strengthening precipitates rich in Al and Ti, such as TiN and Al_4C_3, within the inter-dendritic areas of the weldments [44-45]. The root portion of the FZ exhibits higher hardness compared to the cap portion of the FZ. This is mainly because of the finer grains at the bottom of the FZ which is due to faster cooling that result to higher hardness.

Table 7: Micro-hardness testing result of GTAW welded samples

Position		**Samples**		
	Unit	1	2	2
Cap	HV	168	173	172
Root	HV	171	177	175
Average	HV	169.5	175	173.5

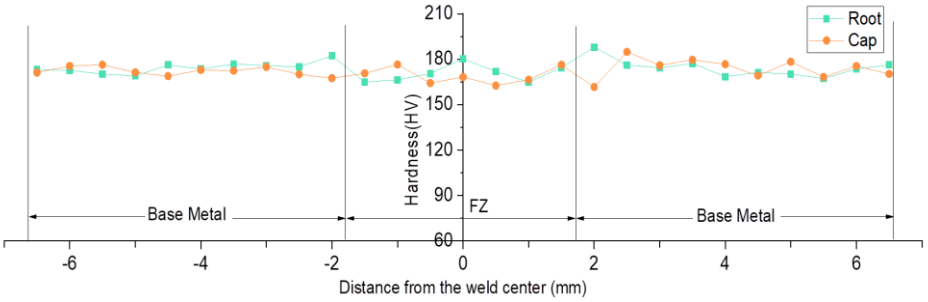

(a)

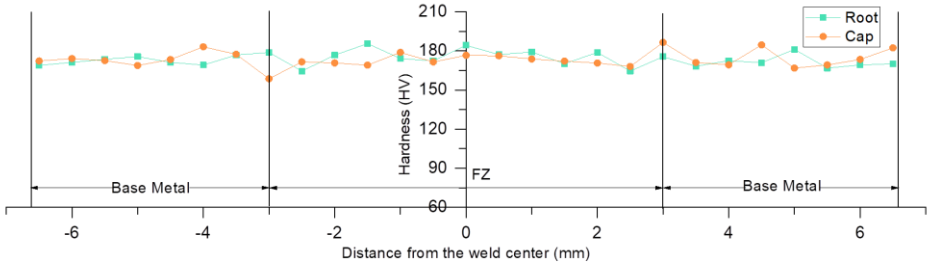

(b)

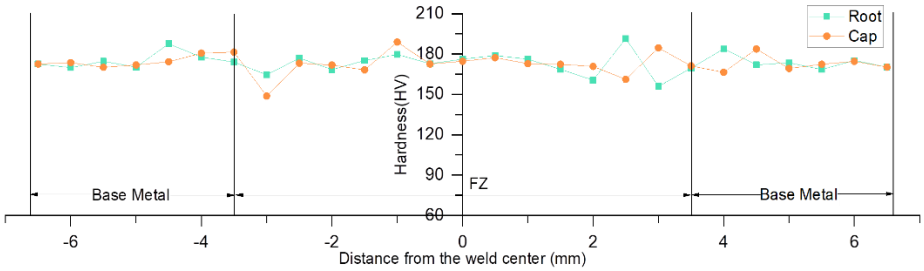

(c)

Figure 16: Micro-hardness profiles of GTAW-welded specimens: (a) for sample 1, (b) for sample 2, and (c) for sample 3.

Figure 17 illustrates the micro-hardness profiles for the EBW samples, and the corresponding outcomes are presented in Table 8. For the EBW welded samples the hardness values were calculated at the cap, middle and bottom portion of the weld samples. Sample 1 exhibit an average fusion zone hardness of 181 HV, 182 HV, and 185 HV at the cap, middle, and root portions, respectively, resulting in an average hardness of 182.67 HV. In the case of sample 2, the cap, middle, and root sections of the weldment exhibit average micro-hardness values of 182 HV, 184 HV, and 190 HV, respectively. Likewise, for sample 3, the cap, middle, and root portions of the weldment display average micro-hardness values of 181 HV, 183 HV, and 186 HV, respectively. The combined average hardness for sample 2 is recorded as 185.33HV while the sample 3 has 183.33HV. Hence, it can be attributed that hardness of base material is softer compared to other zones of weld. This phenomenon can be explained by grain growth occurring from the fusion line towards the centre of the weld, from planner to columnar and then to equiaxed.

Furthermore, as heat input increases, the hardness initially rises and subsequently gradually falls. The rise in hardness can be associated to the existence of Ti-rich precipitates such as TiN and/or secondary phase precipitates such Al_4C_3, which form in the inter-dendritic regions of the weldment [2, 45]. Moreover, when the heat input exceeds a certain threshold, it diminishes the average grain size within the FZ, leading to reduced hardness in the weldments [41, 44]. The root portion of the fusion zone in all three samples exhibits higher hardness compared to the cap portion of FZ. This can be ascribed to the existence of smaller grains at the lower part, which arises from more effective cooling rates in the central and lower portions of the fusion zone. The finer grains contribute to the higher hardness observed in the root portion. [41]. Furthermore, the mean hardness values observed for all EBW-welded specimens exceed those of GTAW-welded samples. This occurrence can predominantly be attributed to various factors associated with the EBW process in contrast to the GTAW process. These

factors encompass reduced heat input, a smaller weld bead geometry, and faster cooling rate in EBW. As a result, the EBW process promotes finer grain growth compared to the GTAW welded samples.

Table 8: Micro-hardness testing result of EBW welded samples

Position		Samples		
	Unit	1	2	3
Cap	HV	181	182	181
Middle	HV	182	184	183
Root	HV	185	190	186
Average	HV	182.67	185.33	183.33

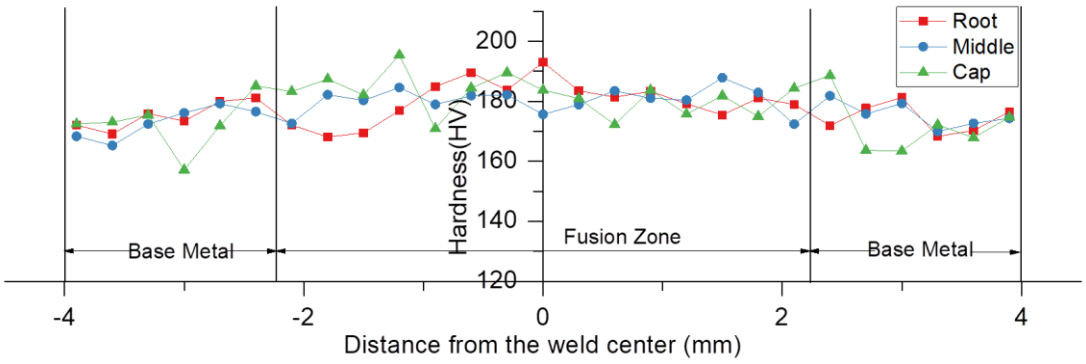

(a)

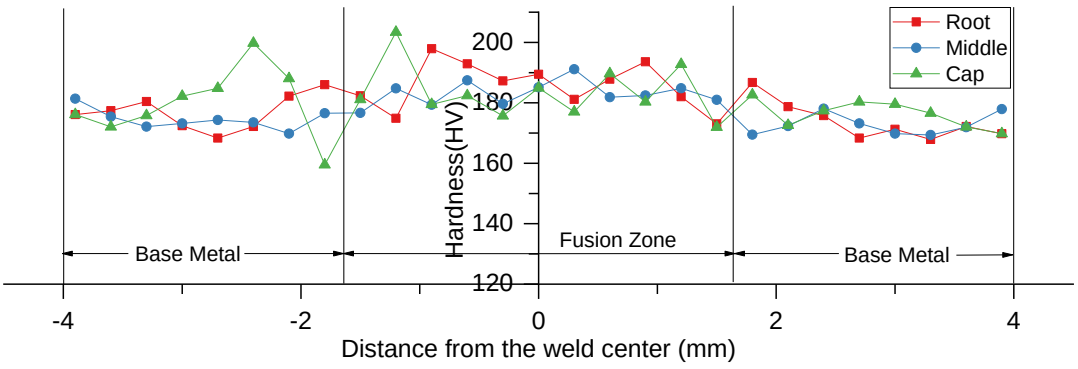

(b)

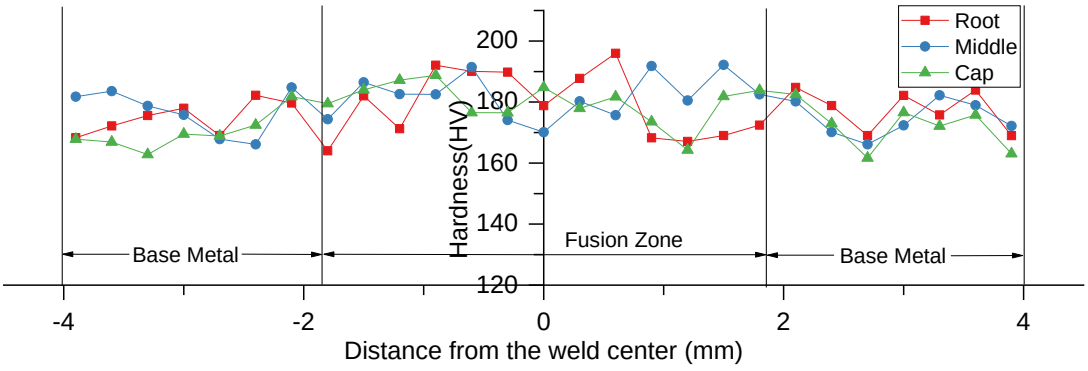

(c)

Figure 17: Micro-hardness profiles of EBW-welded specimens: (a) for sample 1, (b) for sample 2, and (c) for sample 3.

3.6 Tensile properties

The ultimate tensile strength (*UTS*), percentage elongation (%*E*), and yield strength (*YS*) of the Inconel 825 weldments were determined through tensile testing for both the GTAW and EBW processes. The results obtained, along with the fracture positions, are summarized in Table 9. Figure 18 illustrates the changes in mechanical properties for both processes in relation to the heat input.

Table 9: Tensile test result and fracture location

Welding Process	Sample	Heat Input	*UTS* (MPa)	%E (%)	*YS* (MPa)	Fracture Location
GTAW	Sample 1	0.342	578.362	35.00	221.333	Fusion Zone
	Sample 2	0.411	662.016	51.32	231.034	Fusion Zone
	Sample 3	0.468	626.740	43.00	226.387	Fusion Zone
EBW	Sample 1	0.091	432.253	6.92	274.466	Fusion Zone
	Sample 2	0.130	672.896	58.69	285.499	Base metal
	Sample 3	0.184	657.250	57.78	279.852	HAZ

For the GTAW-welded specimens, Sample 1, welded with heat input of 0.342kJ/mm, exhibits a weldment with *UTS* of 578.362 MPa, a *YS* of 221.333 MPa, and 35.0% elongation. This reduced strength compared to the parent metal (654 MPa) is primarily due to insufficient penetration resulting from the lower heat input per unit length of the weldment. For sample 2

welded with a heat input 0.411kJ/mm produces a weld bead of full penetration with *UTS* of 662.016 MPa, *YS* of 231.034 MPa and 51.32% elongation. A further increase heat input to 0.468kJ/mm results a weld bead of *UTS* 626.740 MPa, *YS* of 226.387 MPa and 43% elongation. This lower strength and ductility at higher heat input condition is the result of a slower cooling rate which results in a coarse grain morphology in weld zone of the weldment [41]. This reduction in strength may also attribute due to the presence of solidification crack in the weldment [2-4]. Moreover, the tensile characteristics of the weldments align with the hardness values previously addressed.

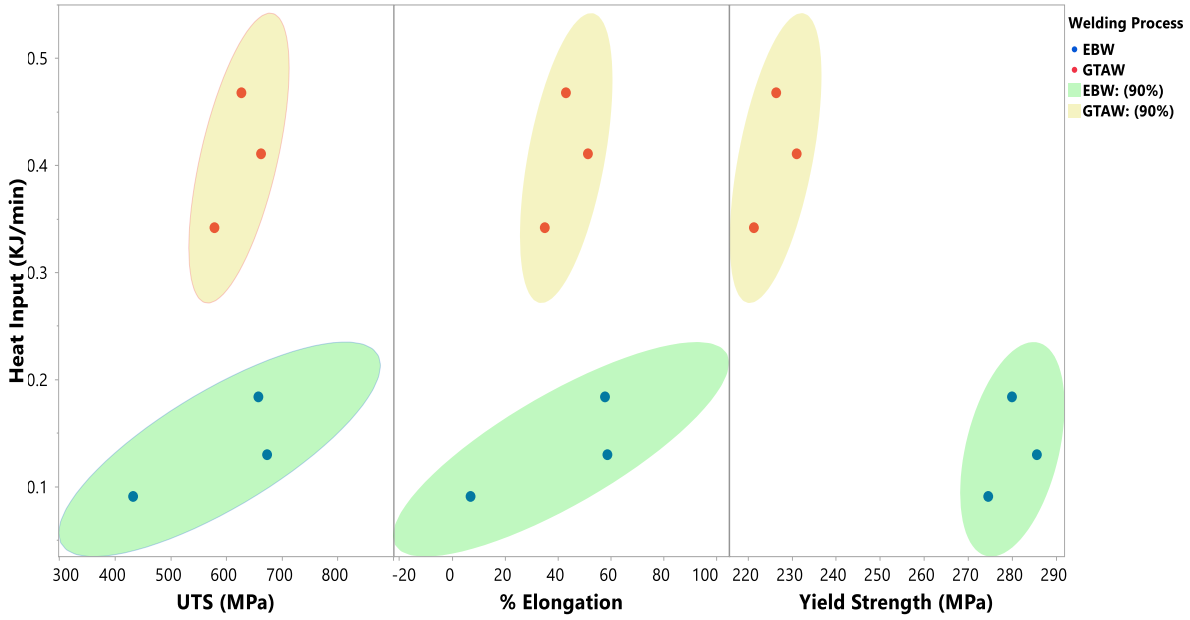

Figure 18: Variation of mechanical properties with respect to heat input

The tensile specimens and the SEM fractograph for the tensile sample 2 and 3 are illustrated in figure 19 and 20 respectively. The fractographs indicates the presence of dimples of varying size which suggest the ductile mode of failure. The density and size of these dimples also has a slight variation with respect to the applied heat input. . Sample 2, with an intermediate heat input of 0.411 kJ/mm, results in more smaller and finer dimples, leading to higher strength and ductility of the weldments. This smaller and finer dimple is attributed mainly due the finer grain morphology in fusion zone. The third sample, subjected to increased heat input, also exhibits the presence of dimples in different sizes; however, these dimples appear slightly coarser, larger, and more elongated. This can be primarily ascribed to the slower cooling rate, resulting in the development of a coarser grain structure within the weld zone.

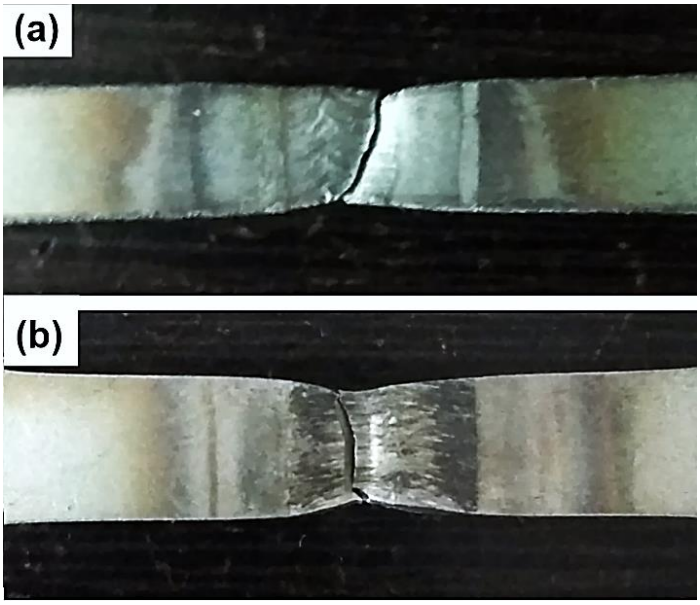

Figure 19: Tensile specimens after fracture for: (a) sample 2; (b) sample 3

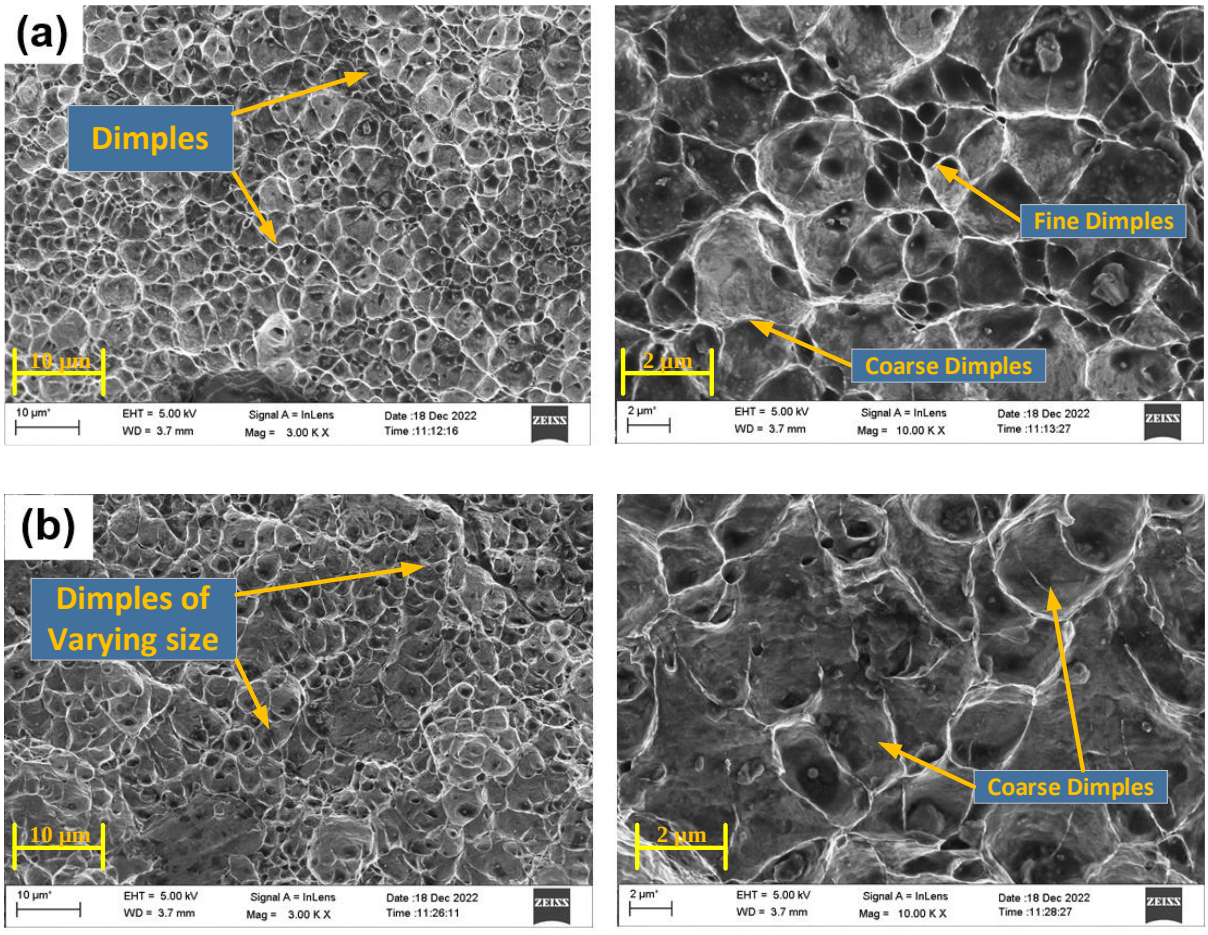

Figure 20: SEM fractographs depicting: (a) sample 2 revealing coarse and fine dimples; (b) sample 3 displaying coarse dimples.

For EBW welded samples, sample 1 welded with heat input 0.091kJ/mm exhibits a weldment with *UTS* 432.253 MPa ,a *YS* of 274.466 MPa and 6.92% elongation. This lower

strength is mainly due to the lack of penetration resulting from the inferior heat input per unit length of weldment. Sample 2, welded with a heat input of 0.130 kJ/mm, produces a weld bead with full penetration, resulting in a *UTS* of 672.896 MPa, a *YS* of 285.499 MPa, and 58.69% elongation. In this instance, the tensile failure occurs at the parent metal, a considerable distance from the fusion zone. Furthermore, increasing the heat input to 0.184 kJ/mm results in the creation of a weld bead with *UTS* of 657.250 MPa, a *YS* of 279.852 MPa, and %*E* of 57.78%. In both sample 2 and 3, the weld zone exhibits either higher or comparable strength to the base metal, which aligns with the hardness values obtained. The enhanced strength can mainly be attributed to the existence of reinforcing elements like Al, Ti, Mn, and Nb, which serve as potent strengthening agents within the weld zone [2-3].

Additionally, as heat input increases, tensile strength initially increases and then declines. This lower strength and ductility at higher heat input is the result of slower cooling rate which results coarse grain morphology in weld zone of the weldments [41]. This reduction in strength may also attribute to the inter-dendritic segregation of Mo, Nb, leading to the creation of detrimental Nb-phase within the weld zone [44, 46]. In comparison, the EBW weldments exhibits better tensile properties than the GTAW weldments. The EBW weldments demonstrate higher values of yield strength compared to GTAW weldments. This increase in YS can be attributed to the combination of a narrow HAZ and finer grain morphology, which promote greater resistance to deformation and yield under applied stress.

Figure 21 illustrates the tensile specimen, while Figure 22 displays fractographs of the tensile samples obtained using SEM. The fractographs of the first sample reveal the existence of both macro and micro-voids, along with clear indications of extensive crack propagation along the grain boundary. This large scale crack propagation is a result of elemental segregation, such as Mo and Nb, or due to incomplete fusion in the weld bead during the conditions of lower heat input. For sample 2 and 3, no such large scale crack propagation are observed in the fractured surface; only a larger area fraction and larger dimensions of micro and macro voids are observed along the fracture surface suggesting ductile mode of failure. This larger number of voids formed by micro-void coalescence (MVC) may attribute due to the presence of precipitates in the microstructure which resulting in the formation of dimple like structure along the fracture surface.

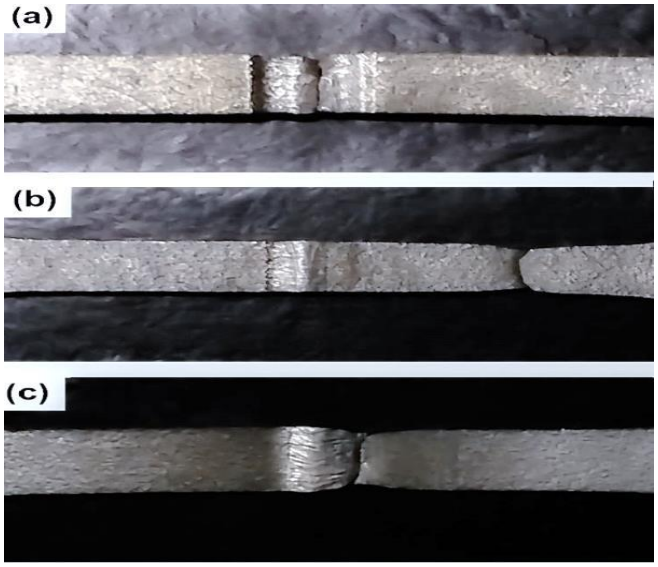

Figure 21: Tensile specimen after fracture for: (a) sample 1; (b) sample 2; (c) sample 3.

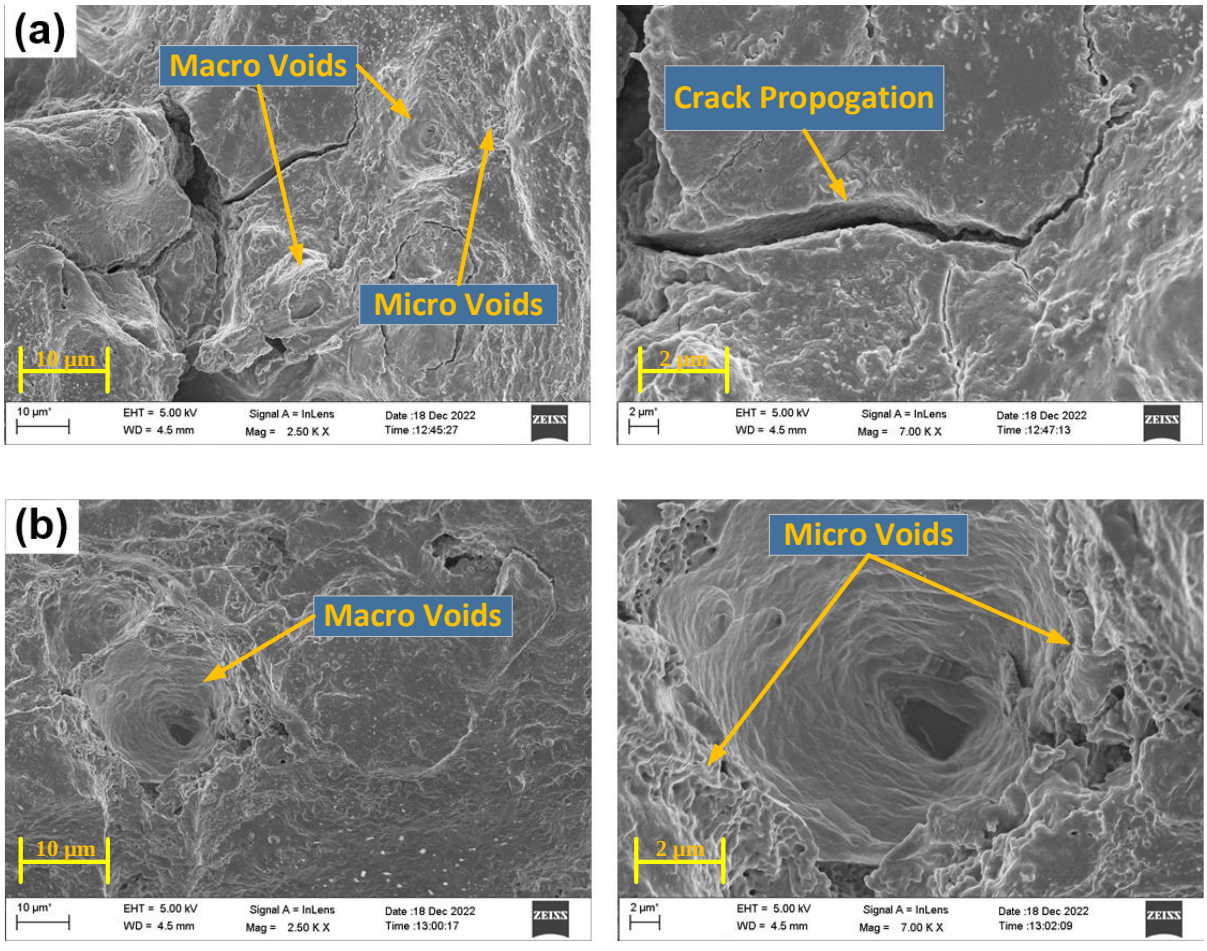

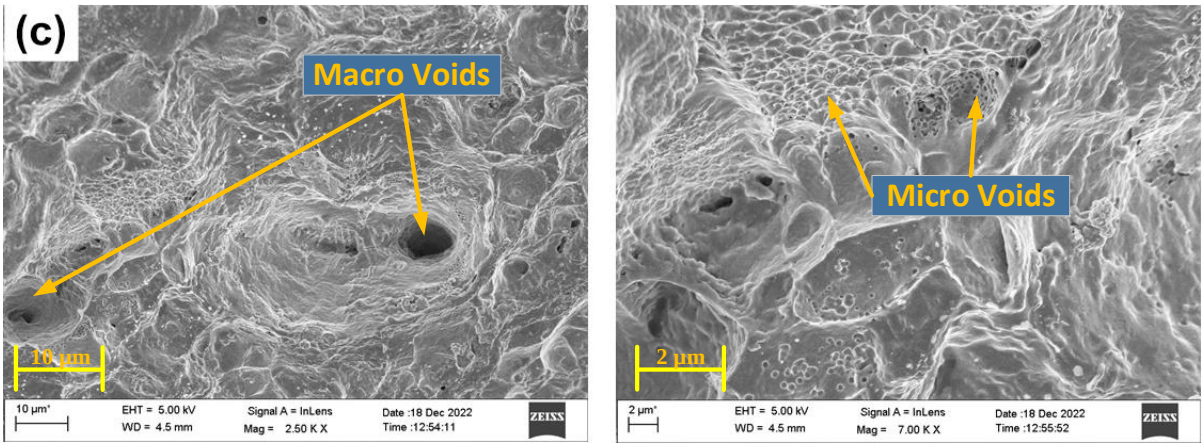

Figure 22: SEM fractographs for: (a) sample 1 depicting large-scale crack propagation with macro and micro voids; (b) sample 2 displaying macro and micro voids; and (c) sample 3 demonstrating macro and micro voids.

Conclusion

This investigation studied the effect of heat input, precipitation and micro segregation of Inconel 825 weldments and compares the effectiveness of GTAW and EBW on Inconel 825 under different operating conditions to determine the most suitable welding technique for this material. The investigation revealed the following outcomes:

1. The quality of the weldments generally improved with increasing heat input, resulting in a reduction in lack of penetration. However, excessive heat input in GTAW resulted in the occurrence of root cracking and solidification cracking. On the other hand, EBW demonstrated better control over undercut and maintained consistent weld quality even at higher heat inputs.
2. Concerning interface morphology, EBW exhibited advantages over GTAW, including reduced HAZ grain growth, absence of detrimental structures, and more uniform heat distribution. EBW demonstrated epitaxial growth and a transition from cellular and columnar dendrites near the fusion line to equiaxed dendrites in the center of the weld, resulting in a fine structure due to accelerated cooling rates.
3. Both GTAW and EBW welded samples exhibit dendritic grain morphologies with distinctive grain boundaries. The presence of SSGBs and SGBs are observed in both welding processes while MGBs is only observed at lower GTAW heat input conditions.
4. Precipitates, such as Al_4C_3 and TiN, are observed in both processes, contributing to improved mechanical properties.

5. In micro segregation study, GTAW weldments showed some degree of segregation for Mo, Cu, Ti, and Al, EBW weldments exhibited negligible segregation for major alloying elements but micro-segregation of Ti and Al.
6. The EBW-welded specimens exhibit superior average hardness when compared to those welded using GTAW. This discrepancy can be ascribed to the reduced heat input, smaller weld bead geometry, and accelerated cooling rate in the EBW process, facilitating the development of finer grains.
7. EBW-welded samples exhibit enhanced tensile strength and ductility compared to GTAW-welded samples. This improvement can be attributed to factors such as lower heat input, smaller (HAZ), faster cooling rate, and reduced rate of elemental segregation in the EBW process.
8. The presence of voids in the fractographs suggests a ductile mode of failure for both GTAW and EBW samples, with variations in void characteristics based on heat input and microstructural features.
9. The comprehensive evaluation of weld bead characteristics, metallurgical properties, hardness values, and tensile properties during EBW of Inconel 825 revealed superior performance compared to Inconel 825 GTAW weldments.

Acknowledgements

The authors extend their gratitude to the institutions of NERIST, IIT Guwahati, and IIT Kharagpur for generously providing the essential resources and facilities essential for conducting this research. SG would like to acknowledge the financial support provided by the UKRI via Grant No. EP/T024607/1, Hubert Curien Partnership Programme from the British Counsil and the International exchange Cost Share award by the Royal Society (IEC\NSFC\223536).

Data Availability

The datasets generated during and/or analysed during the current study are available from the corresponding author on reasonable request.

Conflict of interest

The authors have no conflicts of interest to declare that are relevant to the content of this article.

Declaration of generative AI and AI-assisted technologies

AI and AI-assisted technologies have only been used for readability and linguistic purposes, not for development of any section as such.

Reference

1. Davis, J.R.; and Associates. (2000). Nickel, Cobalt and Their Alloys. ASM speciality handbook. ASM International Materials Park. OH 44073-0002
2. Dupont, J. N.; Lippold, J. C.; Kiser, S. D. (2009). Welding metallurgy and weldability of nickel-base alloys. Hoboken, New Jersey.
3. Caron, J. L.; Sowards, J. W. (2014). Weldability of Nickel based alloys. Elsevier Ltd. Vol 6.
4. Choudhury, B.; Chandrasekaran, M. (2017). Investigation on welding characteristics of aerospace materials – A review. Mater Today: Proceed, 4, 7519-7526.
5. Henderson, M. B.; Arrell, D.; Larsson, R.; Heobel, M.; Marchant, G. (2004). Nickel based superalloy welding practices for industrial gas turbine applications. Sci. Technol. Weld. Join., 9(1), 13-21. DOI: 10.1179/136217104225017099.
6. Patel, D.; Jani, S. (2021). Techniques to weld similar and dissimilar materials by ATIG welding - an overview. Mater. Manuf. Processes, 36(1), 1-16. DOI: 10.1080/10426914.2020.1802040.
7. Sujai, S.; Ramkumar, K.D. (2019). Microstructure and Mechanical Characterization of Incoloy 925 Welds in the As-Welded and Direct Aged Conditions. J. Materi. Eng. and Perform, 28, 1563–1580. https://doi.org/10.1007/s11665-019-03960-0
8. Rodríguez, N. K.; Cortés, R.; Ambriz, R. R.; et al. (2022). Fatigue behavior and microstructural evaluation of Inconel 718 gas tungsten arc welds. Weld World, 66, 145–158. DOI: 10.1007/s40194-021-01190-4.
9. Kumar, P.; Singh, R. K. R.; Sharma, S. K. (2023). Effect of welding parameters on bead characteristics and mechanical properties of wire and arc additive manufactured inconel 718. Proc. Inst. Mech. Eng. Part C: J. Mech. Eng. Sci., 237(7), 1668-1691. DOI: 10.1177/09544062221133035.
10. Srinivas, K.; Kadivendi, V.; Vundavilli, P. R.; Manzoor Hussain, M. (2022). Experimental investigation on microstructural characterization and mechanical properties of plasma arc welded Inconel 617 plates. High Temp. Mater. Processes, 41(1), 683-693. DOI: 10.1515/htmp-2022-0244.
11. Chen, L.; Wei, Y.; Qiu, S.; Zhao, W. (2020). Macro–Micro Scale Modeling and Simulation of Columnar Grain Evolution During Gas Tungsten Arc Welding of Nickel-Based Alloy GH3039. Metall. Mater. Trans. A, 51a, 887.
12. Tork, H. B.; Malekan, M. (2022). Investigating the effect of GTAW parameters on the porosity formation of C70600 copper-nickel alloy. Can. Metall. Q., 62, 180.

13. Xin, Y.; Hua, X.; Wang. M.; Lou, S. (2015). Controlling hot cracking in Ni-based Inconel-718 superalloy cast sheets during tungsten inert gas welding. J. Mater. Process. Technol. 222, 381–390.
14. Kazempour-Liasi, H.; Tajally, M.; Abdollah-Pour, H. (2020). Liquation cracking in the heat-affected zone of IN939 superalloy tungsten inert gas weldments. Int. J. Miner. Metall. Mater., 27, 764–773. DOI: 10.1007/s12613-019-1954-y.
15. Kangazian, J.; Sayyar, N.; Shamanian, M. (2017). Influence of Microstructural Features on the Mechanical Behavior of Incoloy 825 Welds. Metallogr. Microstruct. Anal., 6, 190–199. DOI: 10.1007/s13632-017-0353-x.
16. Kangazian, J.; Shamanian, M. (2018). Mechanical and microstructural evaluation of SAF 2507 and Incoloy 825 dissimilar welds, J. of Mfg. Proc., 26, 407-418. https://doi.org/10.1016/j.jmapro.2017.03.006
17. Sayyar, M.; Shamanian, M.' Niroumand, B.; Kangazian, J.; Szpunar, J.A. (2020). EBSD observations of microstructural features and mechanical assessment of INCOLOY 825 alloy/AISI 321 stainless steel dissimilar welds, J. of Mfg. Proc., 60, 86-95. https://doi.org/10.1016/j.jmapro.2020.10.042
18. Ou, G.; Qian, G.; Jin, H.; Wu, W.; Li, Q. (2022). Microstructure and Corrosion Resistance of Fusion Welding Zone for Duplextubes Welded with Q345R Tube Sheet under Different Welding Currents. Metals, 12, 705. https://doi.org/10.3390/met12050705
19. Gope, D. K.; Chattopadhyaya, S. (2021). Dissimilar Welding of Nickel Based Superalloy with Stainless Steel: Influence of Post Weld Heat Treatment. Mater. Manuf. Process. DOI: 10.1080/10426914.2021.1945095.
20. Bassford, T. H.; Hosier J.C. (1984). Production and Welding Technology of Some High-Temperature Nickel Alloys in Relation to Their Properties, Nuclear Technology, 66:1, 35-43,
21. Ramkumar, K. D.; Mulimani, S. S.; Ankit, K.; Kothari, A.; Ganguly, S. (2021). Effect of grain boundary precipitation on the mechanical integrity of EBW joints of Inconel 625. Mater. Sci. Eng. A, 808, 140926. DOI: 10.1016/j.msea.2021.140926.
22. Vemanaboina, H.; Gundabattini, E.; Akella, S.; Rao, A. C. U. M.; Buddu, R. K.; Ferro, P.; Berto, F. (2021). Mechanical and Metallurgical Properties of CO2 Laser Beam INCONEL 625 Welded Joints. Appl. Sci., 11, 7002. DOI: 10.3390/app11157002.
23. Sujai, S.; Ramkumar, K. D. (2020). Direct ageing response on the microstructure and mechanical properties of electron beam welds of Ni-Cr-Fe alloy used in vacuum insulated tubing. J. Manuf. Processes, 54, 359–373. DOI: 10.1016/j.jmapro.2020.03.027.
24. Arulmurugan, B.; Agilan, M.; Jerome, S.; Arivarasu, M.; Manikandan, M.; Srikanth, S.; Arivazhagan, N. (2018). Investigation of metallurgical and mechanical properties of 21st-century nickel-based superalloy 686 by electron beam welding technique. Sådhanå, 43(2018), 117. DOI: 10.1007/s12046-018-0850-x.

25. Sun, J.; Ren, W.; Nie, P.; Huang, J.; Zhang, K.; Li, Z. (2019). Study on the weldability, microstructure and mechanical properties of thick Inconel 617 plate using narrow gap laser welding method. Mater. Des., 175, 107823. DOI: 10.1016/j.matdes.2019.107823.
26. Arivarasu, M.; Roshith, P.; Padmanaban, R.; Thirumalini, S.; Prabhakar, K. V. P.; Padmanabham, G. (2017). Investigations on metallurgical and mechanical properties of CO2 laser beam welded Alloy 825. Can. Metall. Q., 56:2, 232–244. DOI: 10.1080/00084433.2017.1315847.
27. Srikanth, S.; Parthiban, A.; Ravikumar, M.; Vignesh, K.; (2022). Parameter optimization in Laser Beam Welding for Incoloy 825 Ni-based alloy and AISI 316L steel. Journal of Ceramic Processing Research, 23(4), 523-528. http://dx.doi.org/10.36410/jcpr.2022.23.4.523
28. Muthu, S.M.; Arivazhagan, N.; Rao, M.N. et al. (2022). Oxidation and Hot Corrosion Behaviour of Ni-Based Superalloy 825 and AISI 321 Dissimilar Laser Weldment in K2SO4–60% NaCl Molten Salt Environment at 650°C. Phys. Metals Metallogr. 123, 1306–1316 (2022). https://doi.org/10.1134/S0031918X21100525
29. Mohd Aqeel, S. M.; Shariff, J. P.; Gautam, J.; Padmanabham, G. (2021). Liquation cracking in Inconel 617 alloy by Laser and Laser-Arc Hybrid welding. Mater. Manuf. Processes, 36 (8), 904-915. DOI: 10.1080/10426914.2020.1866200.
30. Yin, X.; He, G.; Meng, W. (2020). Comparison Study of Low-Heat-Input Wire Arc-Fabricated Nickel-Based Alloy by Cold Metal Transfer and Plasma Arc. J. Mater. Eng. Perform., 29, 4222-4232. DOI: 10.1007/s11665-020-04942-3.
31. Ren, W.; Lu, F.; Yang, R.; Liu, X.; Li, Z.; Hosseini, S. R. E. (2015) A comparative study on fiber laser and CO_2 laser welding of Inconel 617. Mater. Des., 76, 207-214.
32. Ruiz-Vela, J. I.; Montes-Rodríguez, J. J.; Rodríguez-Morales, E.; (2019). Effect of cold metal transfer and gas tungsten arc welding processes on the metallurgical and mechanical properties of Inconel® 625 weldings. Weld World, 63, 459-479. DOI: 10.1007/s40194-018-0661-z.
33. Lee, H. T.; Wu, J. L. (2009). The effects of peak temperature and cooling rate on the susceptibility to intergranular corrosion of alloy 690 by laser beam and gas tungsten arc welding. Corros. Sci., 51, 439-445. DOI: 10.1016/j.corsci.2009.01.002.
34. Mohd Aqeel, S. M.; Gautam, J. P.; Shariff, S. M. (2022). Comparative study on autogenous diode laser, CO_2 laser-MIG hybrid and multi-pass TIG welding of 10-mm thick Inconel 617 superalloy. Mater. Sci. Eng. A, 856, 143967. DOI: 10.1016/j.msea.2022.143967.
35. Squillace, A.; Prisco, U.; Ciliberto, S.; Astarita, A. (2012) Effect of welding parameters on morphology and mechanical properties of Ti-6Al-4V laser beam welded butt joints. J. Mater. Process. Technol., 212, 427-436.
36. Fang, X.; Zhang, J. (2014). Effect of underfill defects on distortion and tensile properties of Ti-2Al-1.5Mn welded joint by pulsed laser beam welding. Int. J. Adv. Manuf. Technol., 74, 699-705.

37. Supersedes AWS D17.1:2001. Spec. Fusion Weld. Aerosp. Appl. 2001, American Weld. Soc., FL.
38. Keshavarz, M. K.; Turenne, S.; Bonakdar, A. (2018). Solidification behavior of inconel 713LC gas turbine blades during electron beam welding. J. Manuf. Processes, 31, 232-239.
39. Ren, W.; Lu, F.; Yang, R.; Liu, X.; Li, Z. (2015). Liquation cracking in fiber laser welded joints of Inconel 617. J. Mater. Process. Technol., 226, 214-220.
40. Choudhury, B.; Chandrasekaran, M.; Singh, V.; Ramesh, R. (2023). Optimization of Weld Parameters on Bead Characteristics During EBW of Inconel 825. Advances in Additive Manufacturing and Metal Joining. Lecture Notes in Mechanical Engineering. Springer, Singapore. https://doi.org/10.1007/978-981-19-7612-4_32
41. Kou, S. (2003). Welding Metallurgy, 2nd ed.; John Wiley & Sons: Hoboken, NJ.
42. Avery, R. E.; Tuthill, A. H. (1994) Guidelines for the welded fabrication of nickel alloys for corrosion resistant service. Nickel Development. Institute..
43. Babu, S. S.; David, S. A.; Park, J. W.; Vitek, J. M. (2004). Joining of nickel base superalloy single crystals. Sci. Technol. Weld. Join., 9(1), 1-12.
44. Sohrabi, M. J.; Mirzadeh, H.; Rafiei, M. (2018). Solidification behavior and Laves phase dissolution during homogenization heat treatment of Inconel 718 superalloy. Vacuum, 154, 235-243.
45. Zhang, H.; Huang, C.; Guan, Z.; Li, J.; Liu, Y.; Chen, R.; Wang, Q. (2018). Effects of the Electron Beam Welding Process on the Microstructure, Tensile, Fatigue and Fracture Properties of Nickel Alloy Nimonic 80A. J. Mater. Eng. Perform., 27, 89-98.
46. Mei, Y.; Liu, Y.; Liu, C.; Li, C.; Yu, L.; Guo, Q.; Li, H. (2016) Effect of base metal and welding speed on fusion zone microstructure and HAZ hot-cracking of electron-beam welded Inconel 718. Mater. Des., 89, 964-977.
